Electronic transport and magnetism in the alternating stack of metallic and highly frustrated magnetic layers in Co1/3NbS2

Popčević, Petar; Batistić, Ivo; Smontara, Ana; Velebit, Kristijan; Jaćimović, J.; Živković, Ivica; Tsyrulin, N.; Piatek, J.; Berger, H.; Sidorenko, A.; ...

Source / Izvornik: **Physical Review B, 2023, 107**

Journal article, Published version
Rad u časopisu, Objavljena verzija rada (izdavačev PDF)

https://doi.org/10.1103/PhysRevB.107.235149

Permanent link / Trajna poveznica: https://urn.nsk.hr/urn:nbn:hr:217:594207

Electronic transport and magnetism in the alternating stack of metallic and highly frustrated magnetic layers in $Co_{1/3}NbS_2$

P. Popčević,[1,*] I. Batistić,[2] A. Smontara,[1] K. Velebit,[1,3] J. Jaćimović,[4] I. Živković,[1,4] N. Tsyrulin,[4] J. Piatek,[4] H. Berger,[4] A. Sidorenko,[3] H. Rønnow,[4] L. Forró,[4,5] N. Barišić,[2,3] and E. Tutiš[1,†]

[1]*Institute of Physics, Bijenička c. 46, 10000 Zagreb, Croatia*
[2]*Department of Physics, Faculty of Science, University of Zagreb, Bijenička c. 32, 10000 Zagreb, Croatia*
[3]*Institute of Solid State Physics, TU Wien, 1040 Vienna, Austria*
[4]*Laboratory of Physics of Complex Matter, Ecole polytechnique fédérale de Lausanne, 1015 Lausanne, Switzerland*
[5]*Stavropoulos Center for Complex Quantum Matter, University of Notre Dame, Notre Dame, Indiana 46556, USA*

(Received 3 March 2023; revised 29 May 2023; accepted 6 June 2023; published 29 June 2023)

Transition-metal dichalcogenides (TMDs) are layered compounds that support many electronic phases, including various charge density waves, superconducting, and Mott insulating states. Their intercalation with magnetic ions introduces magnetic sublayers, which strongly influence the coupling between host layers, and feature various magnetic states adjustable by external means. $Co_{1/3}NbS_2$ hosts a particularly sensitive magnetic subsystem with the lowest magnetic ordering temperature in the family of magnetically intercalated TMDs and is the only one where the complete suppression of magnetic order under pressure has been recently suggested. By combining the results of several experimental methods, electronic *ab initio* calculations, and modeling, we develop insights into the mechanisms of electric transport, magnetic ordering, and their interaction in this compound. The elastic neutron scattering is used to directly follow the evolution of the antiferromagnetic order parameter with pressure and temperature. Our results unambiguously disclose the complete suppression of the observed magnetic order around 1.7 GPa. We delve into possible mechanisms of magnetic order suppression under pressure, highlighting the role of magnetic frustrations indicated by magnetic susceptibility measurements and *ab initio* calculations. Electronic conduction anisotropy is measured in a wide temperature and pressure range. Here, we show that the transport in directions along and perpendicular to layers respond differently to the appearance of magnetic ordering or the application of the hydrostatic pressure. We propose a spin-valve mechanism where the intercalated Co ions act as spin-selective electrical transport bridges between host layers. The mechanism applies to various magnetic states and can be extended to other magnetically intercalated TMDs.

DOI: 10.1103/PhysRevB.107.235149

I. INTRODUCTION

Research into transition-metal dichalcogenides (TMDs) is living its second golden age following the first one of the 1970s and 1980s [1,2]. The renewed interest in TMDs is partly driven by fascinating developments in atomically thin layered systems, triggered by groundbreaking experiments on graphene [3–5], and partly due to discoveries of new electronic states in bulk materials [6–12]. Combining the two seems essential for functionalities of quantum devices and future electronics.

The TMDs are quasi-two-dimensional (2D) systems with strong in-plane bonding and weak interlayer coupling. Their electronic system, with effectively reduced dimensionality, is prone to various collective instabilities [1,13]. Moreover, the weak coupling between layers makes TMDs susceptible to intercalation by various atoms and molecules [14,15]. The intercalations with magnetic atoms provide an exciting playground for studying the interplay between conducting electrons and magnetic lattice degrees of freedom [16–23]. This line of research into TMDs has only been partially explored during their first golden age. Nowadays, it is known that such interplays are essential to produce unconventional electronic states, resulting in elaborated electronic phase diagrams and quantum-critical behaviors observed in many families of materials. Notably, it is precisely in this context that superconducting cuprates [24–29], iron pnictides [30–34], and heavy fermion systems [35–39] are often discussed. The advantage of TMDs lies in combining various metallic layers with various magnetic intercalants. Another advantage is the opportunity to fine-tune the coupling between two subsystems by applying relatively modest hydrostatic pressure. In contrast to electronically less anisotropic systems, the magnetic atoms in intercalated TMDs act quite differently in the charge transport in directions parallel and perpendicular to layers. Finally, magnetically intercalated TMDs are known to develop various magnetic phases due to the competition of magnetic couplings of different signs, ranges, and physical origins [14,40–45].

The magnetic order in $Co_{1/3}NbS_2$ appears at a much lower temperature than in other magnetically intercalated TMDs [2]. The ordering temperature T_N (26 K) is ∼6 times lower than the Curie-Weiss temperature θ (157 K), as determined by high-temperature magnetic susceptibility measurements

*ppopcevic@ifs.hr
†etutis@ifs.hr

[40]. This fact alone suggests the significant role of magnetic frustration in $Co_{1/3}NbS_2$. The triangular arrangement of magnetic moments within layers may be partly responsible for the frustration, but this feature is not unique to $Co_{1/3}NbS_2$, as it appears in many other magnetically intercalated TMDs. Several research groups have addressed the magnetic structure in $Co_{1/3}NbS_2$ at ambient pressure, and it was identified as the hexagonal ordering of the first kind (HOFK) [46]. Uncertainties regarding the exact orientation of spins within layers and a possible nonzero average spin perpendicular to layers [2,40,46,47] have also been addressed to a certain extent [11,48]. The large anomalous Hall effect related to this ferromagnetic component of the magnetic ordering has been reported [11,48]. Recently, it was derived from transport measurements that the ordering temperature decreases under pressure, suggesting a possible complete suppression of magnetic order at elevated pressures [49]. This raises the exciting possibility of the quantum spin liquid emerging at those pressures, embedded between metallic layers and stabilized by magnetic interactions mediated by them.

The mechanism of suppressing the antiferromagnetic (AFM) ordering by pressure is also unclear. Several propositions have been made [49]. It was pointed out that the Co magnetic moment can get reduced under pressure. This assumption was partly based on some previous experimental findings and supported by a microscopic argument that Co coupling to metallic states increases under pressure. The alternative is that magnetic frustration becomes decisively important under pressure. The results of this paper bring further clarifications related to both aspects.

Here, we present a collection of experimental and theoretical results aiming to elucidate the physical circumstances and dominant mechanisms acting in $Co_{1/3}NbS_2$. First, we report the elastic neutron scattering measurements that directly address the pressure dependence of the ordering temperature $T_N(P)$, documenting the suppression of magnetic order above the critical pressure $p_c \approx 1.7$ GPa. Second, the previous in-plane transport measurements [49] are now extended above p_c. Third, we present the first measurements of electrical conduction anisotropy in magnetically intercalated TMDs dependent on temperature and pressure. These measurements, aimed to examine the role of magnetic ions in charge transport in directions along and perpendicular to the NbS_2 layers, reveal an unexpected behavior. Fourth, the magnetically ordered state is examined through ac and dc magnetic susceptibility measurements, confirming the presence of the ferromagnetic component. Finally, we analyze our experimental results in the context of our *ab initio* electronic calculations, discerning the effects of intercalation on the electronic structure and their implications on electronic transport. The latter analysis profits from the recent angle-resolved photoemission spectroscopy (ARPES) measurements of the electronic structure [12,50,51].

II. METHODS

Single crystals of $Co_{1/3}NbS_2$ were grown from the vapor phase by iodine transport [2]. The details related to the preparation method are reported elsewhere [40]. The crystal structure of $Co_{1/3}NbS_2$ (shown in Fig. 1) is derived from the one of the parent compound $2H$-NbS_2. Co ions are

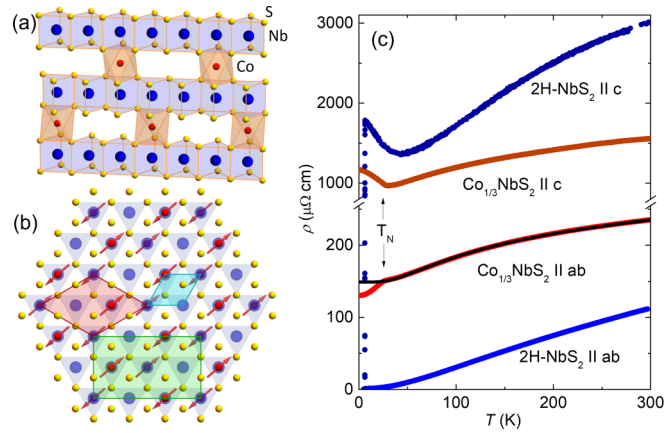

FIG. 1. (a) Schematic of the crystal structure of $Co_{1/3}NbS_2$ along the c axis, with transparent blue and red polyhedra representing trigonal prismatic coordination of niobium and octahedral coordination of cobalt by sulfur, respectively. (b) Schematic of the crystal structure in the ab plane, with blue niobium atoms [only the lower two layers from (a) are shown] depicted as semitransparent to allow for identification of cobalt ions in the lower layer. Red arrows indicate the proposed ordering [46] of Co magnetic moments, with the magnetic moment direction chosen arbitrarily within the plane. The hexagonal order of the first kind (HOFK) is antiferromagnetic (AFM) within the Co layers and in the direction perpendicular to layers. The small cyan rhombus represents the primitive cell of the $2H$-NbS_2 hexagonal unit cell, while the large red rhombus denotes the primitive cell of the crystallographic $Co_{1/3}NbS_2$ hexagonal unit cell. The green rectangle represents the primitive cell of the magnetically ordered $Co_{1/3}NbS_2$ orthorhombic unit cell. The blue trigonal coordination prisms are shown only in one layer. (c) The electrical resistivity of $Co_{1/3}NbS_2$ and its parent compound $2H$-NbS_2 measured in the direction parallel ($||ab$) to NbS_2 layers and along the c axis ($||c$), perpendicular to layers. The black line is the fit to Eq. (1).

intercalated at octahedral sites between NbS_2 layers. They come in a regular triangular planar arrangement, forming the $\sqrt{3}a_0 \times \sqrt{3}a_0$ superstructure, a_0 being the lattice constant of the hexagonal unit cell of the parent compound ($a_0 = 0.331$ nm in $2H$-NbS_2 [52]). $Co_{1/3}NbS_2$ crystalizes in the hexagonal unit cell (space group $P6_322$ and Pearson symbol hP20) [40]. The crystal axis c is perpendicular to the layers, whereas the axes a and b run along the layers.

Unit cell parameters of single-crystal $Co_{1/3}NbS_2$ were determined at room temperature (RT) using an Oxford Diffraction Xcalibur Nova R diffractometer with microfocus Cu tube (Kα line at 1.54184 Å). The data reduction and the calculation of unit cell parameters were made using the CrysAlis PRO program package [53]. Two large platelike single crystals [crystal 1 ($0.50\times0.45\times0.03$ mm^3) and crystal 2 ($0.40\times0.20\times0.02$ mm^3)] were selected for the determination of the unit cell. For both crystals, we collected the diffraction data to a completeness of around 90%. The unit cell parameters were calculated from 217 and 234 reflections for crystals 1 and 2, respectively. It was determined that, at RT, $a = 0.576$ nm and $c = 1.186$ nm. The comparison with the parent compound $2H$-NbS_2 shows that the intercalation weakly affects the NbS_2 planes and their separation [54].

The samples for electrical resistivity measurements were cut into rectangular forms of sizes $1\times0.2\times0.03$ mm^3 and $0.8\times0.8\times0.06$ mm^3, with the smallest dimension being perpendicular to the NbS_2 planes. Gold wires for transport measurements were attached to the crystals using the DuPont silver paste 6838 and cured in a vacuum for 10 min at 200 °C. Electrical resistivity along the c axis (ρ_c) was measured on the larger crystal. For this measurement, the current contacts were painted in a circular form on 20% of the two opposite largest surfaces. Dotlike voltage contacts were painted inside those circles. Much care was invested in the precise alignment of these contacts. Still, the error regarding the absolute value of ρ_c is estimated to be up to 50%. The results for ρ_c in $2H$-NbS_2 and $Co_{1/3}NbS_2$ at ambient pressure were confirmed using focused ion beam sample fabrication [55]. Electrical resistivity under pressure up to 2.5 GPa was measured using the self-clamped piston-cylinder pressure cell. The pressure was monitored *in situ* by measuring the resistance of a standard manganin pressure gauge. The pressure medium used was Daphne oil 7373. The reliability and high precision of the used high-pressure experimental setup were already confirmed in other investigations [56].

The neutron scattering measurements under pressure were performed using the triple-axis spectrometer at Institut Laue–Langevin, Grenoble, using the in-house-made pressure cell [57]. The dc magnetic susceptibility was measured using the superconducting quantum interference device (SQUID) magnetometry in the temperature range 2–300 K and the magnetic field applied parallel or perpendicular to the c axis. The non-SQUID CryoBIND ac susceptibility system [58] was used to measure the ac susceptibility, with the magnetic field (10 Oe rms) applied within the ab plane of the crystal sample.

Ab initio calculations were made using the QUANTUM ESPRESSO package [59], with ultrasoft pseudopotentials from Pslibrary [60]. The kinetic energy cutoff for wave functions was 70 Ry, whereas the kinetic energy cutoff for charge density and potential was 600.0 Ry. We have used the PBE exchange energy functional [61] and the Marzari-Vanderbilt smearing [62] of the Fermi surface (FS) of 0.005 Ry. The Brillouin zone (BZ) sampling used in self-consistent calculations for $2H$-NbS_2 was $19\times19\times5$ k-points (with no shift) and $10\times6\times5$ k-points (with no shift) for $Co_{1/3}NbS_2$. The density of states (DOS) and the FS were calculated using a denser k-point mesh. On-site Coulomb interaction on Co ions was considered within the DFT + U approach proposed by Cococcioni and de Gironcoli [63]. The value of U was obtained from DFT using the linear-response theory [64]. To compare energies of different magnetic ground states, larger kinetic/charge density and potential cutoffs of 90.0/1100.0 Ry were used to obtain consistent results. The crystal structures are relaxed within calculations unless the contrary is stated.

III. EXPERIMENTAL RESULTS

A. Effect of intercalation on electrical resistivity

Regarding the electrical resistivity in the direction perpendicular to layers ρ_c, it is instructive to start from $2H$-NbS_2, where ρ_c is much higher than ρ_{ab}. The anisotropy ρ_c/ρ_{ab}, already substantial at RT $(\rho_c/\rho_{ab})_{\mathrm{RT}} = 27$, rises to a much larger value at low temperatures $(\rho_c/\rho_{ab})_{6\mathrm{K}} = 1300$. This strong temperature dependence of anisotropy in $2H$-NbS_2 is primarily the consequence of much bigger residual resistance in ρ_c than in ρ_{ab}.

Turning to $Co_{1/3}NbS_2$, the c-axis resistivity at RT is two times smaller in the intercalated compound than in the parent compound. The difference in the interlayer distance can be partly responsible, only slightly smaller in the intercalated compound than in the parent compound [65]. The hybridization between Co orbitals and NbS_2 layers also contributes by providing an additional electronic conduction channel. We further discuss this in Sec. IV C and Appendixes A and C, where the electronic structure of the material is examined. Figure 1(c) also shows that the magnetic ordering in $Co_{1/3}NbS_2$ is accompanied by the upturn in $\rho_c(T)$ at Néel temperature followed by a monotonic rise upon further cooling. This increase of resistivity upon spin ordering is counterintuitive to some degree. Generally, one expects the electronic scattering and electrical resistivity to decrease upon reducing the spin disorder. Although the upturn in the electrical resistivity along the c axis is also observed in the parent compound around 50 K, we argue that the minima in $Co_{1/3}NbS_2$ and NbS_2 are caused by very different phenomena. The c-axis resistivity minimum in the parent compound is broad, with the convex resistivity vs temperature curve above and below the minimum. It has been recently ascribed to the unidirectional Kondo-type scattering caused by $1T$-NbS_2 crystal defects in $2H$-NbS_2 [66]. In contrast, the minimum in $Co_{1/3}NbS_2$ is much sharper, occurring only slightly above the ordering temperature of 26 K, with the resistivity vs temperature curve that shows the concave shape in the magnetically ordered state. As announced already, the microscopic origin of the c-axis resistivity in the magnetically ordered state is discussed in Sec. IV C. On the other hand, the expected downturn in resistivity in the magnetically ordered state is found for the in-plane resistivity component $\rho_{ab}(T)$. Note also that the in-plane resistivity increases upon intercalation, resulting in much lower resistance anisotropy in the intercalated system.

B. Effect of pressure on magnetic ordering and electronic transport

The elastic neutron diffraction measurements provide a way to directly verify the effect of the hydrostatic pressure on magnetic ordering. Here, we use the single crystal of $Co_{1/3}NbS_2$ from the same batch as those employed for transport experiments. We identify magnetic peaks that match the magnetic structure determined earlier [46]. The temperature dependence of the intensity of the reflection at [0.5,0.5,0] at ambient pressure, shown in Fig. 2(a), reveals the long-range magnetic order setting in at 26 K. The wave vector, corresponding to the unit cell doubling in the magnetically ordered state, is also the M point of the first BZ (1BZ) of the high-temperature phase. Figure 2(b) shows the variation of scattering intensity around [0.5,0.5,0] at 10 K under pressure, up to the complete disappearance of the signal around 1.7 GPa. The data in Fig. 2 unambiguously demonstrate that the primary claim about the phase diagram of $Co_{1/3}NbS_2$, previously inferred from transport measurements, is correct [49].

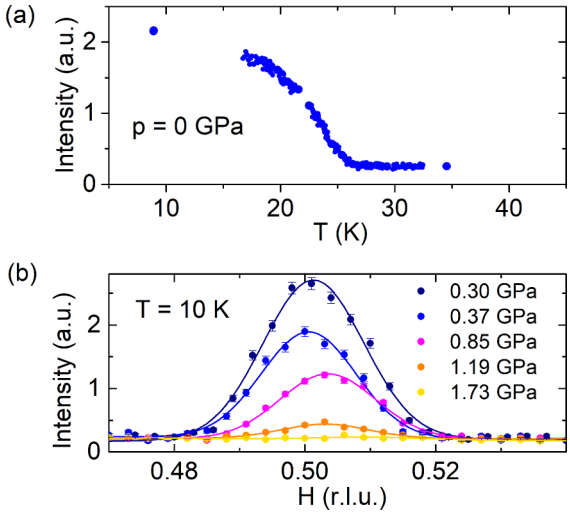

FIG. 2. (a) Temperature dependence of the intensity of the [0.5,0.5,0] magnetic peak at ambient pressure. (b) Pressure dependence of the intensity of the [0.5,0.5,0] magnetic peak at 10 K.

The evolution of in-plane resistivity $\rho_{ab}(T)$ under pressure up to 1.6 GPa has already been described in Ref. [49]. There, the magnetic ordering temperature was related to the minimum in $(\frac{d\rho_{ab}}{dT})$. Here, we extend the transport measurements under pressure by measuring resistivity in the direction perpendicular to layers ρ_c and by expanding the pressure range well above the critical value.

Figure 3 shows that, in the pressure range between 1.7 and 2.36 GPa, $\rho_{ab}(T)$ becomes progressively more featureless

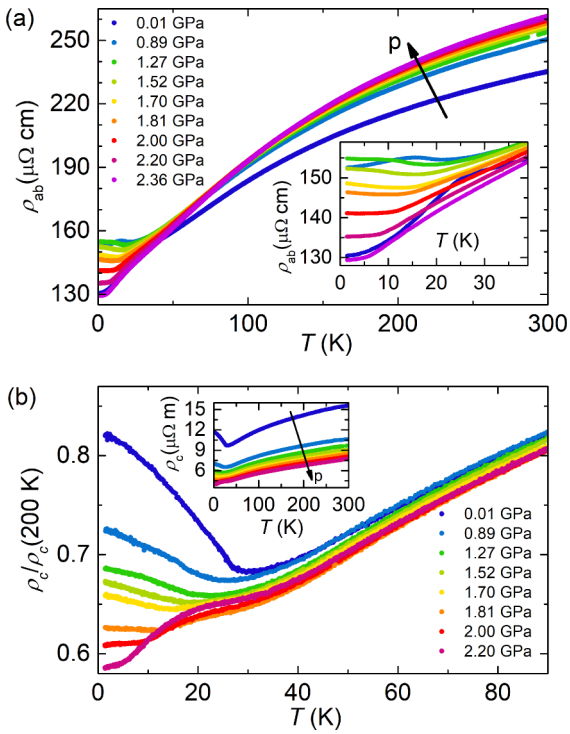

FIG. 3. The electrical resistivity of $Co_{1/3}NbS_2$ measured (a) in the *ab* plane (ρ_{ab}) and (b) along the *c* axis (ρ_c) measured at different pressures in the 1.5–300 K temperature range.

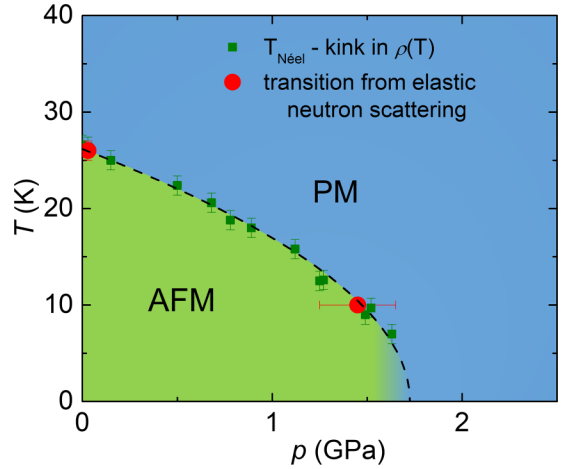

FIG. 4. Phase diagram of $Co_{1/3}NbS_2$ under pressure. The green portion represents the AFM phase, while the blue represents the paramagnetic (PM) phase. The green squares represent the inflection point of the electrical resistivity curve $\rho_{ab}(T)$; the red circles mark the phase transition obtained from elastic neutron scattering. The dashed curve represents the simple square root fit to the dependence of the transition temperature on pressure, as described in the main text.

below 30 K and acquires the ordinary metallic temperature dependence at higher pressures. In the pressure range between 2.0 and 2.4 GPa, we have extended our measurements to 60 mK, motivated by previous findings of superconductivity in the vicinity of the magnetically ordered phase [7,8,30,67]. However, no superconductivity was observed in the pressure range just quoted or at any other point in the investigated pressure-temperature phase diagram.

Interestingly, the changes in ρ_{ab} and ρ_c induced by pressure are opposite in sign in the wide high-temperature range between 50 and 300 K. It can also be noted that the upturn in $\rho_c(T)$, related to magnetic ordering at ambient pressure, diminishes upon raising the pressure. The temperature of minimum steadily declines under pressure. The minimum persists to pressures slightly above 1.7 GPa, and $\rho_c(T)$ maintains multiple inflections in the low-temperature region even at higher pressure.

Based on these experimental results, we present the extended *p*-*T* phase diagram of $Co_{1/3}NbS_2$ in Fig. 4. The $T_N(p)$ dependence shown there is obtained from $\rho_{ab}(T)$ dependences at various pressures. For this purpose, we prefer using $\rho_{ab}(T)$ curves over $\rho_c(T)$. This is because the minimum in ρ_c is located at slightly higher temperature than determined by the neutron scattering at ambient pressure and seems to result from the competition of at least two opposing mechanisms. Thus, the minimum marks the temperature where one mechanism prevails over the other, representing a less precise way to determine the ordering temperature from the electric transport data. The simple square root dependence can describe the pressure dependence of the magnetic transition temperature: $T_N(p) = a\sqrt{p_0 - p}$. From the fit of the data presented in Fig. 4, we obtain critical pressure to be $p_0 = (1.72 \pm 0.02)$ GPa and ambient pressure Néel temperature $T_N(0) = a\sqrt{p_0} = (26.17 \pm 0.02)$ K.

C. Magnetic susceptibility and frustration

Figure 5(a) shows our results for the magnetic susceptibility of $Co_{1/3}NbS_2$ measured below RT. The two curves correspond to configurations with the magnetic field of 1 T oriented parallel and perpendicular to the c axis. In both cases, the susceptibility follows, from the highest measured temperature to below 100 K, the Curie-Weiss law $\chi(T) = \chi_0 + C/(T-\theta)$. As usual, χ_0 represents the temperature-independent contribution resulting from diamagnetism and Pauli paramagnetism, C stands for the Curie constant, and θ is the Curie-Weiss temperature [68]. For a system with identical magnetic ions, the Curie constant is given by their concentration n and the square of their magnetic moment $\langle\vec{\mu}^2\rangle$, $C = n\langle\vec{\mu}^2\rangle/3k_B$. Using the concentration of Co ions in $Co_{1/3}NbS_2$ for n, our measurements yield $\sqrt{\langle\vec{\mu}^2\rangle} = (3.17 \pm 0.03)\mu_B$, $\theta = (-170 \pm 5)$ K, and $\chi_0 = (0.6 \pm 0.5)\times 10^{-4}$ emu/mol Oe for the magnetic field applied parallel to the ab plane and $\sqrt{\langle\vec{\mu}^2\rangle} = (3.13 \pm 0.05)\mu_B$, $\theta = (-160 \pm 5)$ K, and $\chi_0 = (1.5 \pm 0.5)\times 10^{-4}$ emu/mol Oe applied along the c axis. These values correspond rather well to those reported earlier [11,40,47].

The Curie-Weiss temperature is much higher than the magnetic ordering temperature, with the factor of frustration $|\theta|/T_N > 6$, corroborating the assumption of strong magnetic frustration [69]. The magnetic frustration in $Co_{1/3}NbS_2$ may partly come from the triangular arrangement of Co within the Co sublayers [32]. On the other hand, the competing magnetic couplings reaching beyond the nearest neighbors may also contribute to the large factor of frustration.

The inset in Fig. 5(a) shows the difference in the magnetic susceptibility measured in field-cooled (FC) vs zero-field-cooled (ZFC) regimes with the magnetic field pointing along the c axis [70]. In Fig. 5(b), we also present ac magnetic susceptibility measurements that show transition at 26 K accompanied by a substantial signal below the transition temperature. The latter indicates the ferromagnetic character of the ordered state. This we attribute to canting of magnetic moments along the c axis, simultaneously occurring with their AFM ordering. Consequently, the appearance of the ferromagnetic component also provides a simple explanation for the observed large anomalous Hall effect [11], which seems unique to Co-intercalated TMDs [11,71,72]. It is worth emphasizing that the ferromagnetic canting of AFM-ordered magnetic moments usually results from antisymmetric exchange [Dzyaloshinskii-Moriya (DM)] contribution to the magnetic exchange interaction [73]. That points to superexchange [74] as the relevant interaction mechanism between Co magnetic moments in $Co_{1/3}NbS_2$. Notably, the DM interaction is held responsible for the helical magnetic order in the isostructural sister compound $Cr_{1/3}Nb\ S_2$ [44,45,75].

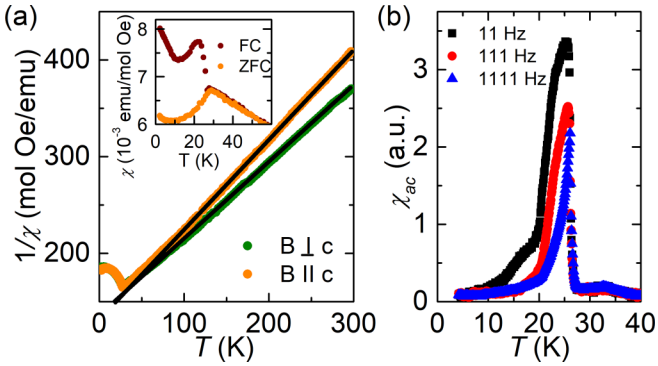

FIG. 5. (a) The magnetic susceptibility measured in the zero-field-cooled (ZFC) regime. The measurements were conducted with a 1 T magnetic field oriented in the ab plane (olive circles) and along the c axis (orange circles). Black lines are fits to the Curie-Weiss law, as explained in the text. Inset: Magnetic susceptibility in field-cooled (FC, dark red circles) and ZFC (orange circles) regimes measured using 0.1 T magnetic field oriented along the c axis, (b) ac magnetic susceptibility measured at frequencies of 11, 111, and 1111 Hz in the field of 1 mT rms.

IV. DISCUSSION AND THEORETICAL CONSIDERATIONS

A. Understanding electronic transport

Here, we start with the temperature dependence of the in-plane resistivity $\rho_{ab}(T)$, which shows concave curvature between 50 and 300 K. Similar concave behavior in electrical resistivity has been observed in several other systems, such as A15 superconductors [76,77], some spinel and skutterudite compounds [78–80], the filled cage compounds [81], and the Kondo lattice systems [82]. The common feature appearing in the explanations of such behavior is an effective dynamic disorder that scatters electrons and grows upon heating but saturates above some energy/temperature scale. The concave behavior in resistivity is usually parametrized by extending the usual Bloch-Grüneisen relation by a phenomenological term with thermally activated behavior [76]:

$$\rho_{ab}(T) = \rho_0 + \rho_1\left(\frac{T}{\theta_D}\right)^n \int_0^{\theta_D/T} dx \frac{x^n e^x}{(e^x-1)^2} + \rho_2 e^{-T_0/T}, \tag{1}$$

where θ_D and T_0 represent the Debye temperature and characteristic temperature for thermal activation of disorder, respectively. The relation in Eq. (1) fits the temperature dependence of the in-plane resistivity observed in $Co_{1/3}NbS_2$ at ambient pressure very well. The fitting provides $\theta_D = (400 \pm 30)$ K, in accordance with previous reports [49,83], $n = 3$ [84]. The last term in the relation in Eq. (1) is responsible for the concave behavior, with the parameter $T_0 = (130 \pm 10)$ K, of the same order of magnitude as the Curie-Weiss temperature θ found in magnetic measurements (Sec. III C). Consequently, T_0 is also the temperature scale that marks the loss of spatial correlation among magnetic moments. The concave curvature around and above T_0 appears as the precursor of the saturation of the electronic scattering on the maximal spin disorder in the high-temperature limit. Our interpretation is like the one proposed for filled cage compounds [81], where the rattling atoms, loosely bound within the crystal structure, oscillate within their cages. When fully thermally agitated, these atoms no longer contribute to the rise of configuration entropy. We also note that the temperature scale comparable with T_0 marks the minimum of the Seebeck coefficient in $Co_{1/3}NbS_2$ [49].

The concave curvature in $\rho_{ab}(T)$ remains preserved under pressure. Figure 6(a) shows excellent fits of the relation in

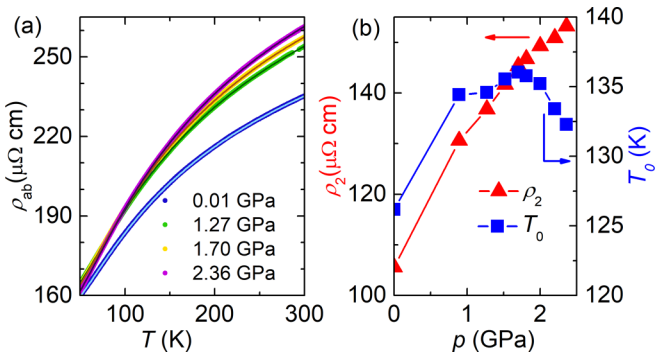

FIG. 6. Electrical resistivity at different pressures fitted above 50 K using the relation in Eq. (1). (b) Evolution of the ρ_2 and T_0 parameters under pressure.

Eq. (1) to experimental data of Fig. 3(a) in the temperature range between 50 and 300 K. The evolution of the parameters ρ_2 and T_0 under pressure is shown in Fig. 6(b). The parameter ρ_2, which stands for coupling of conducting electrons to magnetic disorder, exhibits a monotonic increase under pressure. In comparison, the characteristic energy scale T_0 shows nonmonotonic pressure dependence. Incidentally, the maximum of T_0 correlates with the pressure at which the AFM order is suppressed. Notably, the determined Debye temperature shows the expected increase under pressure, whereas the coupling ρ_1 [84] does not change significantly.

Equation (1) does not address the low-temperature features in $Co_{1/3}NbS_2$, with deviations between experimental data and fits to Eq. (1) starting to show below 50 K. Apart from the reduction of the ordering temperature under pressure, the resistivity exhibits complex temperature/pressure behavior. Several minima and maxima in $\rho_{ab}(T)$ develop below 20 K and additional inflection points in $\rho_c(T)$. These features point to multiple low energy scales, possibly related to separate scattering mechanisms on quasidegenerate magnetic configurations in a frustrated magnetic system [85]. Complex magnetic textures of $Co_{1/3}NbS_2$ have been suggested recently, even at ambient pressure, as the source of the large anomalous Hall effect [11]. Further experimental research is required to determine the evolution of spin dynamics upon varying temperature and pressure, where inelastic neutron scattering and nuclear magnetic resonance appear promising approaches.

In contrast to the in-plane resistivity at RT, the resistivity along the c axis decreases under pressure. The changes of opposite signs signify the different roles of Co atoms in electronic transport in two directions. In both cases, the changes are probably governed by the amplification of coupling between Co orbitals and itinerant electrons of the NbS_2 layers. For in-plane transport, where the spin disorder on Co atoms acts primarily as the scattering source, the amplified coupling under pressure leads to higher resistivity. Conversely, in the c-axis direction, where Co atoms act as bridges between layers, the resistivity decreases as the coupling improves under pressure. This view also explains the big change in the residual resistivity along the c-axis direction under pressure. Further discussion of the electronic transport along the c axis is presented in Sec. IV C, upon addressing the electronic structure.

B. Calculations of the electronic structure in the magnetically ordered state

The simplest approach to the electronic structure of intercalates is to assume that the electronic bands of the host material remain rigid upon intercalation. The parent compound $2H$-NbS_2 features fully occupied sulfur p bands and half-filled niobium d bands, which account for its metallic properties [86]. The bonding within layers is covalent, whereas the cohesion is much weaker between layers, often considered to originate from the van der Waals forces. The charge transfer is expected between the intercalated ions and the conduction bands of the host, increasing their filling level. In $Co_{1/3}NbS_2$, this charge transfer has been previously argued to be one electron [40] or two electrons per Co atom [2]. The electrons left in crystal-field-split Co $3d$ orbitals are assumed to form dispersionless bands. These electrons localized on Co $3d$ orbitals are responsible for the magnetic moment of Co ions.

In the more realistic approach, the number of electrons transferred from the Co atom to NbS_2 layers is a noninteger, whereas the hybridization between Co orbitals and NbS_2 planes is finite [12] and affects the physical properties of $Co_{1/3}NbS_2$ in several ways. As we will show, the intercalation governs most of the physical processes and properties addressed in this paper, including the electric interlayer transport and the intralayer scattering of electrons, and affects the magnetic coupling between Co ions to some extent. The calculations and considerations presented in what follows explore the consequences of these hybridizations and interactions in more detail.

Ab initio electronic structure computations for pristine and $2H$-NbS_2 intercalated by 33% Co have been recently reviewed in Ref. [12] in conjunction with the ARPES study of the electronic structure. Most importantly, the electronic structure calculations in $Co_{1/3}NbS_2$ must account for the big magnetic moment on Co ions. This property is experimentally verified through magnetic susceptibility obeying the Curie-Weiss law in the wide temperature range above the magnetic ordering temperature. It was also verified in the magnetically ordered state through neutron scattering measurements [46]. This magnetic moment of the Co ion is difficult to catch in DFT calculations in the nonmagnetic state or without properly accounting for the Coulomb repulsion within the Co d orbitals. The need to address strong electron repulsion within d orbitals in the *ab initio* calculations of the electronic structure of Co-based compounds is also evident from previous works [87–89], where the DFT + U method has been tested and recommended. The value of $U = 5$ eV, which we obtained from DFT using the linear-response theory [64] in $Co_{1/3}NbS_2$, is consistent with those works [12]. The comparison with electronic structure calculations in the magnetic state without U shows that $U = 5$ eV significantly affects the distribution of electrons across Co orbitals and produces the value of the Co magnetic moment closer to the one determined experimentally here. On the other hand, our investigation shows that the electronic structure close to the Fermi level is not very susceptible to small variations of U around the 5 eV value.

It was shown that the DFT + U calculations [12] in $Co_{1/3}NbS_2$, conducted in the magnetically ordered state,

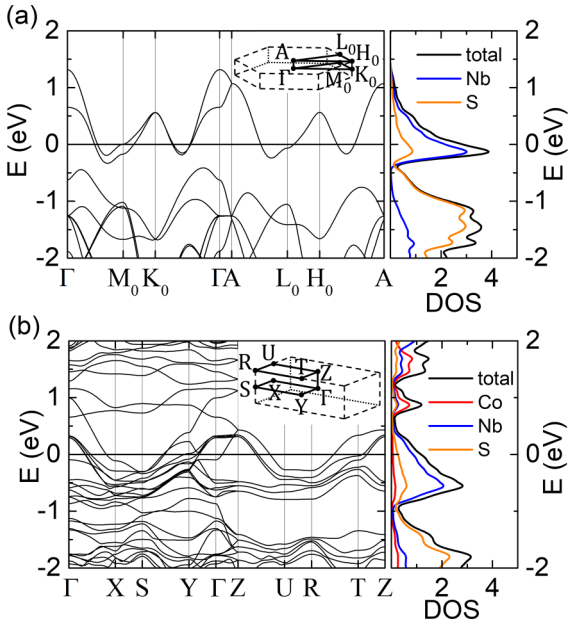

FIG. 7. Band structure for (a) $2H$-NbS_2 and (b) $Co_{1/3}NbS_2$. The Fermi energy corresponds to $E = 0$.

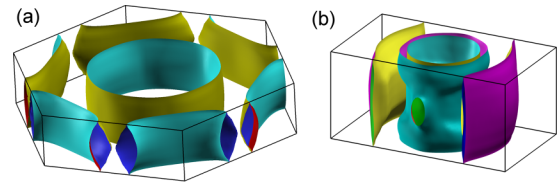

FIG. 8. Fermi surfaces of (a) $2H$-NbS_2 and (b) $Co_{1/3}NbS_2$.

reproduce very well the most dispersive bands around the Fermi level measured in ARPES [12,50,51]. The feature at the Fermi level observed by ARPES in $Co_{1/3}NbS_2$ that DFT + U cannot catch is the shallow and weakly dispersive band presumably related to Co orbitals [12,50,51]. The observed feature, also identified in the sister compound $Cr_{1/3}Nb\,S_2$ [90,91], is interesting from a fundamental point of view [12]. However, it is probably of secondary interest regarding the intercalation-induced effects on electric transport, where the changes in highly dispersive bands are expected to play the primary role. Thus, in this section, we concentrate on the differences between the DFT-calculated band structures of $2H$-NbS_2 and $Co_{1/3}NbS_2$, shown in Fig. 7.

As expected, the calculated electronic structure of $Co_{1/3}NbS_2$ inherits much from the electronic structure of $2H$-NbS_2 [92]. Notably, the band structure of the single NbS_2 layer (not shown) is characterized by a single conduction band dominantly composed of Nb orbitals. Correspondingly, the electronic structure of the $2H$-NbS_2 crystal, with two layers contributing to the unit cell, has two such bands near the Fermi level, as shown in Fig. 7(a). These bands run as quasidegenerate throughout most of the k-space. The splitting between two bands, produced by the interlayer hybridization, maximizes around the Γ point, whereas no splitting occurs on the topmost surface of the 1BZ, at $k_z = \frac{\pi}{c}$. Both bands cross the Fermi level twice between the Γ and K points, resulting in the FS sections shown in Fig. 8(a).

The crystallographic unit cell in $Co_{1/3}NbS_2$ is threefold bigger, with the additional doubling of the unit cell occurring upon the AFM ordering. The unit cell in AFM-ordered $Co_{1/3}NbS_2$ thus contains 12 Nb atoms, 24 S atoms, and 4 Co atoms. The electronic band structure of $Co_{1/3}NbS_2$ remains relatively simple near the Fermi energy, with only six bands crossing the Fermi level. The computed FSs for both compounds can be compared in Fig. 8. Notably, the sixfold enlargement of the unit cell in real space, corresponding to a sixfold smaller 1BZ in $Co_{1/3}NbS_2$ than in $2H$-NbS_2, does not result in the proliferation in the number of FS segments, as one would naively expect. As discussed in more detail in Appendix A, the first reason for the relative simplicity of the calculated FS in $Co_{1/3}NbS_2$ lies in the absence of Co-dominated bands appearing at the Fermi level. The second reason lies in the shrinking of the FS pockets around the Γ and K_0 points within the original 1BZ due to increased conduction band filling. These small pockets get preserved upon folding the FS of doped $2H$-NbS_2 into the 1BZ of $Co_{1/3}NbS_2$ (Appendix A).

The DFT results show an amplified separation between the two original conduction bands at the Γ point, indicating increased interplane hybridization upon Co intercalation. As a result, the bonding band becomes submerged below the Fermi level at the Γ point, leading to a band crossing the Fermi level along the ΓZ direction in Fig. 7(b). This crossing contrasts with the absence of such a crossing along the ΓA direction in the parent compound in Fig. 7(a). The evolution of this band is the key factor behind the change in the FS from a quasi-2D cylinder [Fig. 8(a)] to a 3D potlike shape, central to Fig. 8(b) (better visualized in Fig. 10), in agreement with the ARPES results [12]. The bottom of the pot represents the portion of the FS where the Fermi velocity is oriented along the z axis and corresponds to the band crossing the Fermi level along the ΓZ direction in Fig. 7(b). Hence, we attribute the reduction of the electrical resistivity along the c axis and lower resistivity anisotropy in $Co_{1/3}NbS_2$ to this feature in the electronic structure.

One way to investigate the reasons for bigger effective hybridization between Nb layers in $Co_{1/3}NbS_2$ is the following: First, the overlap between Co orbitals and orbitals of niobium and sulfur atoms provides the covalent bonding between layers, which is not present in the parent material. This additional binding is the probable reason for reducing the interlayer distance upon intercalation, contrary to what one would usually expect to happen. Second, the reduced interlayer distance also affects the direct hybridization between NbS_2 layers. The relative importance of the two mechanisms is not easy to quantify. Comparing the band structure of relaxed $2H$-NbS_2, the band structure of $Co_{1/3}NbS_2$, and the band structure of NbS_2, where the spatial arrangement of Nb and S atoms are identical as in $Co_{1/3}NbS_2$ (detailed in Appendix B), may help in that regard. The last of these band structures indicates that the second mechanism is important but insufficient to fully account for the splitting between bonding and antibonding Nb 4d bands in $Co_{1/3}NbS_2$. Further hybridization with the orbitals of the intercalated Co ions, caught by the DFT calculation in the intercalated material, is required to push the bonding band

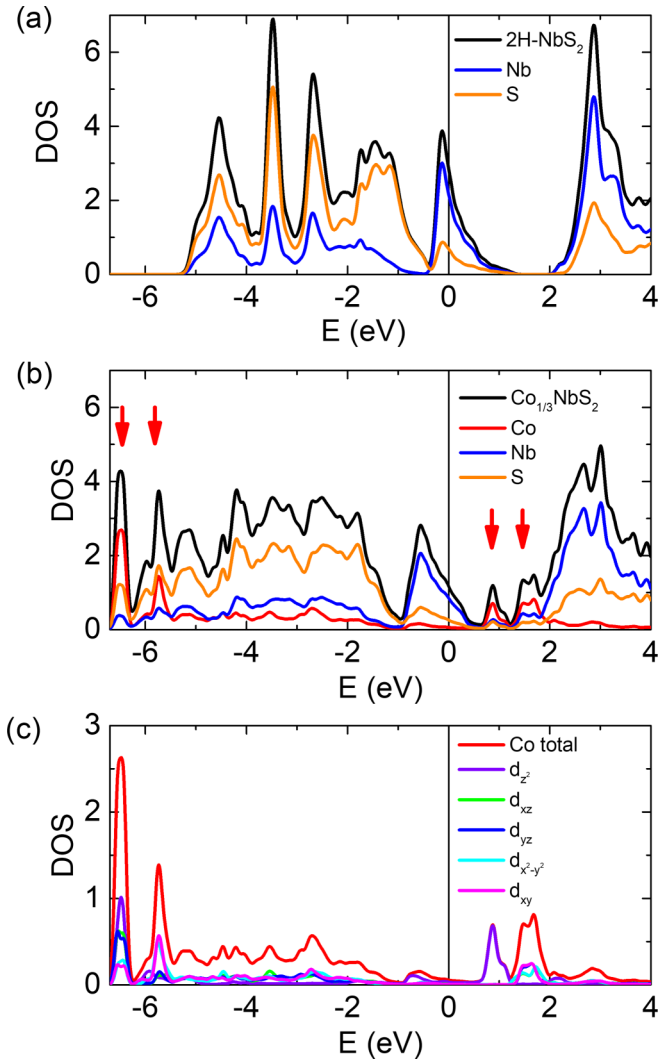

FIG. 9. The density of states (DOS) as calculated for (a) $2H$-NbS_2, (b) $Co_{1/3}NbS_2$, and (c) projected on different Co orbitals. Red arrows in (b) mark positions where most of the Co DOS is positioned. To keep the graphs for two compounds easily comparable, the units used in graphs correspond to the number of states per unit energy per unit cell divided by the number of Nb atoms within the unit cell. The origin of the energy scale is set to E_F.

below the Fermi level. The latter hybridization also reflects in the sizable contribution of Co orbitals to the wave functions of the bonding band around the Γ point.

The contribution of various atoms and orbitals to the electronic structure can also be viewed through the projected DOS in $2H$-NbS_2 and $Co_{1/3}NbS_2$, shown in Figs. 9(a)–9(c).

The part of the spectrum around the Fermi energy in Fig. 9(a) is split in half by the Fermi level, justifying the half-filled conduction band qualification for $2H$-NbS_2. The corresponding part of the spectrum for $Co_{1/3}NbS_2$, shown in Fig. 9(b), is similar in shape but differently positioned relative to the Fermi level. The position of the Fermi level in $Co_{1/3}NbS_2$ corresponds to $\frac{5}{6}$ filling of the conduction band and seems to justify the assumed charge transfer of 2 electrons from the Co ion into the NbS_2 layers, suggested earlier [2,41,86].

The contribution of Co orbitals is dominantly positioned in parts of the DOS spectra far from the Fermi level, as indicated by red arrows in Fig. 9(b). This separation primarily results from crystal field splitting and electronic correlation effects. Still, the cobalt contribution is visible in the conduction bands. Regarding the contribution relative to other types of atoms, it is essential to emphasize that only one cobalt orbital (Co $3d_{z^2}$) contributes significantly to this energy range against three niobium and numerous sulfur orbitals.

A closer look at the conduction bands in $Co_{1/3}NbS_2$ and $2H$-NbS_2 also reveals that the conduction band section of the spectrum has a bigger energy extension in $Co_{1/3}NbS_2$ than in $2H$-NbS_2. The widening of the conduction band originates mainly from the bigger interlayer hybridization, where Co orbitals contribute significantly. What is not visible from Fig. 9 is that Co orbitals contribute mainly to one out of several bands and in a particular part of the k-space. This can be more easily observed in Fig. 10, where the contributions from all types of atoms to various bands at the FS are visualized using the Fermisurfer viewer [93]. The lowest row in Fig. 10 shows the contribution of the bonding band to the FS. The cobalt contribution is most significant in the bonding band, as shown in the last column of Fig. 10, maximizing at the bottom of the potlike FS of the bonding band. This indicates the pivotal role of the Co orbitals in the c-axis conduction and electrical anisotropy reduction upon intercalation.

However, the participation of the Co orbitals in the conduction band leads to noninteger occupancy of the Co $3d$ orbitals. In our *ab initio* calculations, this occupancy is determined to the value of ∼7.5. The noninteger charge transfer is also reflected in the Co magnetic moment, to be discussed next.

The projection of the magnetic moment along the magnetization direction obtained from our DFT calculations in the magnetically ordered ground state is $\langle\mu_\alpha\rangle_{\mathrm{DFT}} = 2.36\mu_B$ per Co ion. This is 21% smaller than the value expected for a standalone magnetic ion with $S = \frac{3}{2}$ and $g = 2$: $\langle\mu_\alpha\rangle = g\mu_B S = 3\mu_B$. The effective spin reduction from $\frac{3}{2}$ to 1.18 is the consequence of the hybridization of Co $3d$ orbitals with the Nb and S orbitals in the crystal and with the conduction band states. Using 1.18 instead of $\frac{3}{2}$, one can calculate the effective magnetic moment $\mu_{\mathrm{eff}} \equiv \sqrt{\langle\vec{\mu}^2\rangle} = 2\mu_B\sqrt{\langle S(S+1)\rangle} = 3.21\mu_B$, which features in the Curie-Weiss formula for high-temperature magnetic susceptibility [68]. This value is only 1% larger than the measured value $(\sqrt{\langle\vec{\mu}^2\rangle})_{\mathrm{exp}} = 3.17\mu_B$ (see Sec. III C) [94]. Thus, the DFT calculation accounts well for the magnetic moment measured in the high-temperature, magnetically disordered state.

It is also worth reconciling the Co magnetic moment here with the charge occupancy of the Co $3d$ orbitals of 7.5, discussed above. Such an occupancy would imply a magnetic moment of $2.5\mu_B$, provided that the first Hund rule applies. This rule is indeed obeyed within our DFT results regarding the positions of the energy levels of Co $3d$ majority- and minority-spin orbitals relative to the Fermi level. The value of $2.36\mu_B$ is the consequence of majority-spin $3d$ orbitals on Co not being fully occupied due to their small participation in band states above the Fermi level.

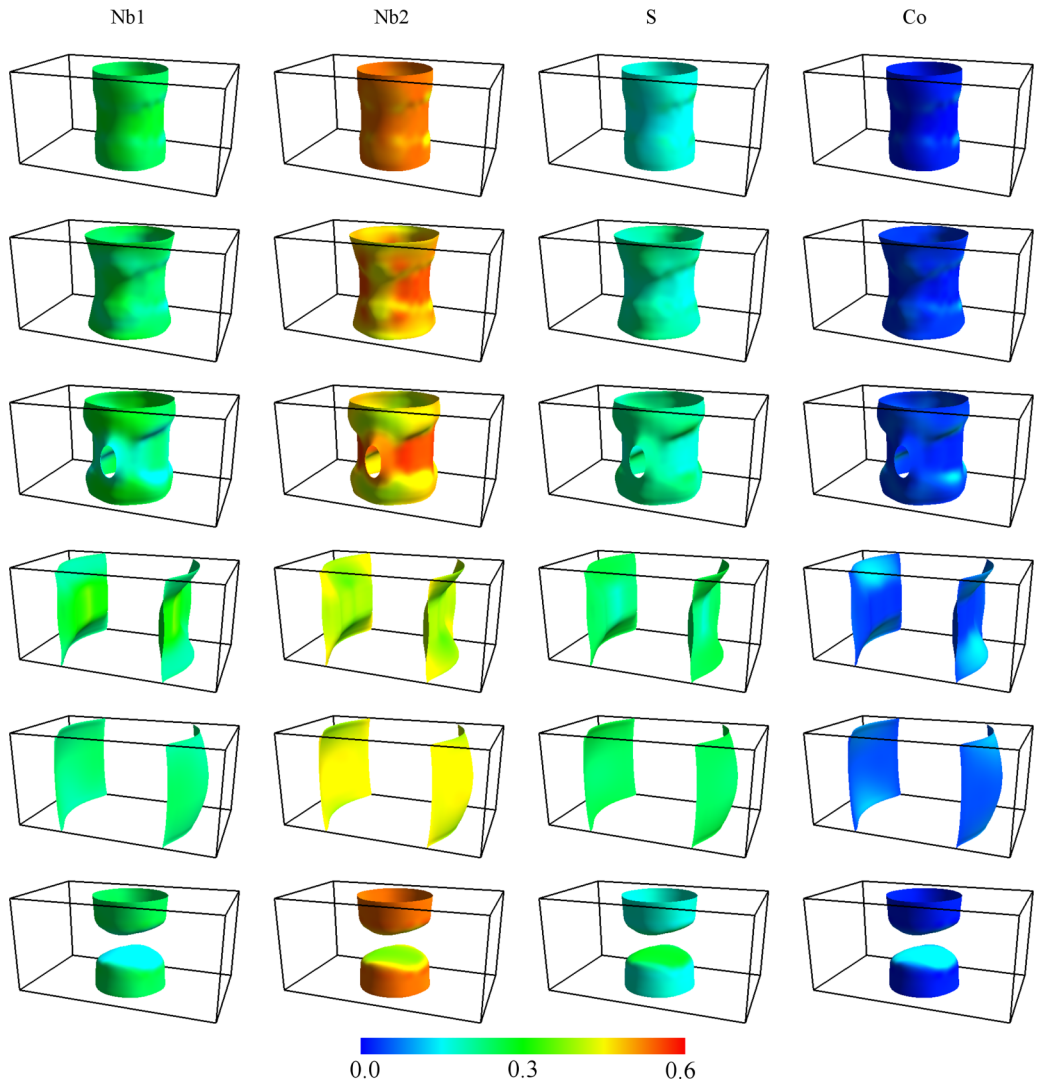

FIG. 10. The share (projection) of atomic orbitals (d orbitals for Nb and Co atoms and p orbitals for S atom) in the electronic states at the Fermi surface of $Co_{1/3}NbS_2$. Nb2 stands for the niobium atoms closest to Co ions, whereas the share of other niobium atoms is denoted by Nb1.

Finally, we estimate the compressibility along the *ab* plane from the experimentally observed shifts of Bragg peaks under pressure. It amounts to 0.004 GPa^{-1}. The experimental setup did not permit us to determine the compressibility along the c axis. For comparison, the experimentally estimated compressibility for the sister compound $Cr_{1/3}Nb\,S_2$ amounts to 0.0022 GPa^{-1} in the *ab* plane and 0.039 GPa^{-1} along the c axis [95]. The calculated compressibility of $Co_{1/3}NbS_2$ amounts to 0.00302 GPa^{-1} in the *ab* plane and 0.00767 GPa^{-1} along the c axis. Thus, in magnetically intercalated TMDs, the compressibility along the c axis is about twice as large as in-plane compressibility [95,96]. The ratio is much smaller than in the parent compound, where the compressibilities for the two directions differ by one order of magnitude [97]. The reduced compressibility ratio indicates the transition from van der Waals to ionic/covalent bonding between layers upon intercalation. This reduction might be viewed as the mechanical counterpart to the reduced electrical anisotropy discussed above.

C. Spin valve regulated interplanar electronic transport

A recent study [12] quantifies the increase in the effective hybridization between metallic Nb layers upon Co intercalation. It also indicates that this hybridization amplification is locally spin selective. Those findings are based on ARPES measurements and several types of electronic structure calculations. Here, we qualitatively evoke those findings and employ them to understand the effect of magnetic ordering on the electric transport along the c-axis direction.

Here, we start from the Co ion in the $3d^7$ electronic state with the +2 charge and $S = \frac{3}{2}$, appropriate when Co orbitals do not hybridize with surrounding atoms but experience their crystal field. In that state, within the appropriate basis, only three Co $3d$ orbitals, approximately half-filled, participate in forming a $\frac{3}{2}$ magnetic moment of Co. Out of three orbitals, one of them (Co $3d_{z^2}$) will dominantly hybridize with states forming the conduction band within the NbS_2 layer (that is, the Nb $4d$ orbitals and surrounding sulfur orbitals) [12], as witnessed in Fig. 9(c). This hybridization is the primary

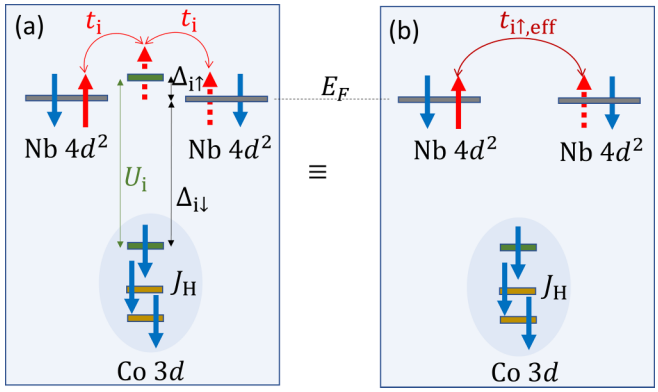

FIG. 11. The figure shows the electrons hopping between two Nb $4d$ orbitals of neighboring layers utilizing the Co $3d_{z^2}$ orbitals (represented by green bars) of the intercalated cobalt atom. For simplicity, only a few other Co $3d$ orbitals are shown, represented by light brown bars. The spin state of the Co atom is approximately $S = \frac{3}{2}$, as ruled by the effective Hund coupling (J_H) between electrons in Co $3d^7$ configuration. In the figure, we consider the Co atom is in the $S_z = -\frac{3}{2}$ spin state. The spin-down Co $3d$ orbitals are occupied in this state, positioned deeply below the Fermi level (E_F), whereas the energy levels of some spin-up Co $3d$ orbitals remain empty and above the Fermi level. (a) This situation opens the possibility for spin-up electrons to hop between Nb $4d$ in neighboring layers using the unoccupied Co $3d_{z^2}$ spin-up orbital lying close above E_F. The hybridization between the Nb $4d$ orbital and the Co $3d_{z^2}$ orbital of the intercalated atom is denoted by t_i, whereas the energy separations between energy levels of the orbitals involved are denoted by $\Delta_{i\uparrow}$ for spin-up (and $\Delta_{i\downarrow}$ for spin-down) orbitals. Since $\Delta_{i\downarrow} \gg \Delta_{i\uparrow}$ for the assumed spin state of Co, the effective Co-assisted interlayer tunneling for spin-up electrons is much more efficient than for spin-down electrons, $t_{i\uparrow,\mathrm{eff}} \gg t_{i\downarrow,\mathrm{eff}}$. Only the former is shown in (b) as an effective Nb-Nb hybridization caused by the Co atom. A similar picture applies to Co in $S_z = +\frac{3}{2}$ spin state, with spin-up and spin-down symbols getting interchanged. The drawing does not account for the direct Nb-Nb hybridization.

source of the observed departure of the Co ion from the ideal $S = \frac{3}{2}$ state.

The local Coulomb repulsion between spin-up and spin-down electrons in the Co $3d_{z^2}$ orbital is strong, partly represented by the U parameter in DFT calculations. Consequently, the Co $3d_{z^2}$ orbital is occupied by an electron of one spin projection (e.g., spin-down), with its energy lying well below the Fermi level. The electronic state for the electron of opposite spin projection (spin-up) within the same orbital is positioned above the Fermi level and stays empty in an ideal case. However, this last state is positioned within the 1 eV range above the Fermi level, whereas its hybridization t_i with states forming the conduction band is of the order of 0.3 eV [12]. Thus, the Co atom in the spin-down state greatly increases the local hybridization between nearby Nb layers for spin-up electrons. The opposite happens for the Co atom in the spin-up state, which locally amplifies the local interlayer hybridization for spin-down electrons. The effective hybridization between Nb layers is thus significantly larger than the hybridization between Nb layers in pure $2H$-NbS_2.

The interplanar conduction is illustrated in Fig. 11. The spin-up electron (shown in red) is hopping between two Nb $4d$ orbitals in neighboring layers, virtually utilizing the Co $3d_{z^2}$ spin-up state orbital of the intercalated atom. The average spin-down state of the Co $3d_{z^2}$ orbital is maintained through the effective Hund coupling (J_H) to other electrons in Co $3d$ orbitals. Thus, the spin-up electrons can hop only via the spin-down Co bridges and vice versa. Equivalently, each Co ion can be regarded as a spin-valve regulating interlayer electronic transport. The distribution of spin-up and spin-down spin valves depends on the magnetic state. In the AFM HOFK state of $Co_{1/3}NbS_2$, the arrangement of Co ions obstructs the transport along the c-axis direction. Essentially, the distribution of spin valves reduces the possibility for an electron of a given spin projection to use the nearest Co orbitals for transport between layers, forcing further in-plane detours instead. That effectively increases the resistivity in the magnetically ordered state compared with the magnetically disordered state, where a bigger probability exists of finding a closer appropriate bridge. The schematic drawings for the two cases are presented in Appendix C.

D. On mechanisms of suppression of the magnetic order with pressure

Some mechanisms for suppression of the AFM ordering under pressure were proposed in the previous study [49]. Here, we address those scenarios considering our new experimental findings and *ab initio* calculations. The first scenario was motivated by the observation of strong dependence of Co magnetic moment μ on the concentration x of intercalated cobalt in Co_xNbS_2, accompanied by the systematic variation of the c-axis lattice constant $c(x)$ [47]. As x varies from 0.3 to 0.2, the jump in the Co spin was reported, with S diminishing from $\sim\frac{3}{2}$ to below 1, accompanied by the observed decrease of the c-axis lattice constant. The correlation allows for the causal relationship between the value of the c-axis lattice constant and the Co magnetic moment. This causal relationship extends to the scenario where the Co magnetic moment gets reduced under pressure in $Co_{1/3}NbS_2$. On the other hand, our DFT + U calculations for pressurized material at $x = \frac{1}{3}$ show that, up to hydrostatic pressure of 2 GPa, the magnetic moment of the Co ion decreases less than 2% from its ambient pressure value. Thus, the DFT + U calculations do not reproduce the large decrease of the Co magnetic moment, leaving the possibility that the Co magnetic moment gets heavily screened through processes not accounted for by these calculations.

The Kondo-type screening comes to mind as a possibility, alongside Doniach's mechanism for magnetic ordering collapse [98]. To recall, the Doniach phase diagram explores the competition between magnetic ordering, characterized by the ordering temperature T_N, and the Kondo screening, characterized by the temperature T_K. In Doniach's picture, where the Ruderman-Kittel-Kasuya-Yosida (RKKY) interaction governs the magnetic ordering, T_N and T_K depend on the magnetic coupling J_0 between the local magnetic moment and conduction electrons. As the coupling J_0 increases, the suppression of magnetic ordering occurs when the AFM-ordering temperature T_N, $T_N \propto J_{RKKY}$, $J_{RKKY} \propto g_F J_0^2$, becomes inferior to the Kondo temperature $T_K \propto E_F e^{-\mathrm{const.}/J_0 g_F}$, with g_F denoting the electronic DOS at the Fermi level and E_F denoting

the depth of the occupied metallic band. The collapse of the magnetic ordering then arises due to the pressure-induced increase of the coupling J_0.

There are several objections regarding the dominant role of the RKKY interaction in the magnetic ordering in $Co_{1/3}NbS_2$. The first relates to the ferromagnetic component observed in the magnetically ordered state. As discussed in Sec. III C, this observation indicates the presence of the DM coupling, which is impossible to capture within the RKKY scheme. The biggest objection related to the role of the RKKY as the dominant magnetic interaction in $Co_{1/3}NbS_2$ comes from the predominantly AFM character of the interlayer coupling, a benchmark of the observed HOFK magnetic state. Within RKKY, the interaction between the closest Co ions of the neighboring Co layers goes through the NbS_2 metallic layer that they share. It is the biggest RKKY interaction in the system, and it is ferromagnetic. The ferromagnetic nature of the RKKY interaction at distances $d < 1/k_F$ is the general feature of RKKY. In our case, d stands for the distance between the coupling points of two Co ions to the NbS_2 layer between them, and k_F represents the typical Fermi wave number for the doped NbS_2 layer. The particularities of the electronic structure of NbS_2 layers and the particularities of the Co coupling to metallic states do not change that. The details of the calculations within particular models are provided in Ref. [99].

Irrespective of the precise nature of the dominant interaction between magnetic moments, the Kondo-type screening of magnetic moments by conduction electrons remains a way to collapse magnetic ordering. The sizable reduction of the $S = \frac{3}{2}$ spin state, discussed above in relation to our *ab initio* calculations, already witnesses the presence of the strong coupling of the Co magnetic moment and conducting electrons. Addressing the Kondo-type screening in $Co_{1/3}NbS_2$ requires going beyond the DFT calculations. The recent ARPES observation of signals at the FS, not foreseen by the DFT + U calculations, signals the possibility of strong electron correlations effects playing an important role in $Co_{1/3}NbS_2$ and similar magnetic intercalates [12,50,51,90,91]. It is theoretically established that $S = \frac{3}{2}$ can be effectively Kondo screened, either fully or partially (underscreening), depending on the number of coupled screening channels [100–103]. Spatially selective partial Kondo screening was also suggested as a possible scenario in highly frustrated Kondo lattice systems [104]. In this respect, we note that magnetic susceptibility under pressure might help to clarify remaining issues related to the Co spin state.

Finally, we come to the scenario where magnetic frustration is responsible for the collapse of the magnetic ordered state. The total energy calculation of various magnetically ordered states appears as a possible way to compare various magnetic configurations theoretically. This route was essentially taken by Polesya *et al.* [105] using DFT. However, the tripling of the unit cell upon magnetic ordering, claimed there, is not observed experimentally.

At this point, it should be stated that the DFT calculations in $Co_{1/3}NbS_2$ produce only tiny differences between total energies (per formula unit) of various magnetically ordered states. As may be expected, these differences lie within the $k_B T_N \ll \theta$ range. For example, we have calculated the energies of HOFK magnetically ordered and ferromagnetically ordered states at ambient pressure. The energy of the HOFK state is lower by only 8.665×10^{-5} Ry per magnetic unit cell, which roughly corresponds to 14 K. Moreover, as specified in the Methods section, these calculations require unusually large energy and wave vector cutoffs to produce consistent results. The tiny differences in energy qualitatively indicate the quasidegeneracy of various magnetic configurations. Notably, the in-plane electrical resistivity in Fig. 3 shows an increase in the residual resistivity upon approaching the critical pressure. Also, a certain minimum develops in a limited pressure range. These complex behaviors are likely the result of this competition among different ground states and the balance between them that is affected by pressure.

On the other hand, the recent study of electronic structure in $Co_{1/3}NbS_2$ [12] shows that DFT cannot reproduce certain bands observed at the Fermi level, even qualitatively, thus our low confidence in DFT to correctly reproduce the fine energy differences between various magnetic configurations. The theoretical approaches beyond standard DFT calculations must be developed and applied to $Co_{1/3}NbS_2$ to understand its magnetic ordering from the first principles. Consequently, magnetic frustration remains a valuable candidate for understanding how the hydrostatic pressure leads to the complete suppression of the magnetic order in $Co_{1/3}NbS_2$. The quasidegeneracy in energy between various magnetic states, being already present to a large extent at ambient pressure, can experience an additional boost under pressure. That allows for thermal and quantum fluctuations keeping the system magnetically unordered to the lowest temperatures.

V. CONCLUSIONS

Our elastic neutron scattering experiments confirm the suppression of AFM ordering in $Co_{1/3}NbS_2$ above 1.7 GPa, indicated earlier by transport measurements. In magnetically intercalated TMDs, we measure the electrical resistivity under pressure in the direction perpendicular to layers, demonstrating the unusual rise in resistivity upon entering the magnetically ordered phase. Being related to magnetic ordering, the upturn disappears as the magnetic order is suppressed by pressure. We propose spin-selective Co-assisted transport between layers as a primary reason for the observed phenomenon. Our magnetic susceptibility measurements at ambient pressure and low temperature confirm the canting of ordered Co magnetic moments, pointing to finite DM interaction and the relevance of exchange interactions in $Co_{1/3}NbS_2$.

Several mechanisms of suppression of magnetic ordering under pressure have been explored in this paper. Concerning our findings, some mechanisms were discarded and some scenarios advanced and refined, with the verdict still pending. The RKKY interaction is eliminated as the dominant interaction between magnetic moments. The Kondo-type screening of magnetic moments escapes our observations but remains a candidate for the collapse of the magnetic ordering under pressure. Another viable candidate is the increased magnetic frustration under pressure, whose presence at ambient pressure is quantified through our experimental results and high cutoff DFT calculations.

Further experimental and theoretical work may be required to fully understand the nature of the magnetic state and its disappearance under pressure in $Co_{1/3}NbS_2$. The same is likely to apply to other magnetic intercalates of TMDs.

ACKNOWLEDGMENTS

This paper was supported by the Unity through Knowledge Fund, under Grant No. 65/10, Croatian Ministry of Science, Education and Sports Grants No. 035-0352826-2848 and No. 035-0352826-2847, Croatian Science Foundation Projects No. IP-2016-06-7258 and No. IP-2020-02-9666, and by the project Cryogenic Centre at the Institute of Physics–KaCIF cofinanced by the Croatian Government and the European Union through the European Regional Development Fund-Competitiveness and Cohesion Operational Programme (Grant No. KK.01.1.1.02.0012). The work at TU Wien was supported by FWF Project No. P27980-N36 and the European Research Council (Consolidator Grant No. 725521). The work at EPFL was supported by Sinergia grant "Mott physics beyond the Heisenberg model" of the Swiss NSF. Authors acknowledge Yuki Utsumi (Institute of Physics, Zagreb) for helpful discussions about band structure and Krešimir Molčanov (Institute Ruđer Bošković, Croatia) for determining lattice parameters of $Co_{1/3}NbS_2$.

APPENDIX A: BAND STRUCTURE EVOLUTION THROUGH FOLDING

Figure 7(a) shows two Nb 4*d* bands crossing the Fermi level in $2H$-NbS_2 and forming FSs shown in Fig. 8(a). In Fig. 8(b), six FSs are shown in $Co_{1/3}NbS_2$, with one of them showing a pronounced 3D character and dispersion along the k_z axis. If the rigid band approximation would hold for states primarily composed of niobium and sulfur orbitals, the FS in $Co_{1/3}NbS_2$ should emerge from $2H$-NbS_2 bands upon two simple transformations.

The first step in understanding the FSs in $Co_{1/3}NbS_2$ [Fig. 8(b)] involves accounting for the charge transfer of ∼2 electrons per Co ion into the NbS_2 planes, which requires shifting the Fermi level in the parent compound. The resulting FSs are then folded from the initial hexagonal 1BZ of $2H$-NbS_2 into the sixfold smaller orthorhombic 1BZ of AFM-ordered $Co_{1/3}NbS_2$. This folding process is illustrated in Fig. 12, where the folding occurs in two steps. First, the large hexagonal BZ of $2H$-NbS_2 is folded into the smaller hexagonal BZ of crystallographic $Co_{1/3}NbS_2$, corresponding to the superperiodicity imposed by Co intercalation. Second, the small hexagonal BZ of crystallographic $Co_{1/3}NbS_2$ is folded into the orthorhombic BZ of magnetically ordered $Co_{1/3}NbS_2$, which reflects the superperiodicity occurring upon magnetically ordering the magnetic moments of the Co ions. Thus, in Fig. 12(b), we fold the second and third BZs of hexagonal $Co_{1/3}NbS_2$ to obtain six cylindrical FSs: four smaller ones around the Γ point, coming from the K_0 points of Fig. 12(a) and two larger ones already present in Fig. 12(a). The second folding goes from the hexagon drawn in red in Fig. 12(b) into the twofold smaller BZ represented by the rectangle drawn in green in Fig. 12(c). As visible from Figs. 12(b) and 12(c), only the large orange circles are affected by the last folding. The final result, shown in Fig. 12(c), contains six FS segments arising from six bands.

The comparison of the folding results and the electronic structure for $Co_{1/3}NbS_2$ of Figs. 7(b) and 8(b) permits us to spot the main effect of the intercalation on the electronic dispersion: Fig. 12(c) contains six FS segments, arising from six bands, whereas the electronic structure results for $Co_{1/3}NbS_2$ accounts for only five FS segments crossing the $k_z = 0$ plane. The corresponding five bands closely resemble the bands found in $2H$-NbS_2. Figure 10, produced through the Fermisurfer software [93], shows all the sections of the FS through the 1BZ and resolves the mystery of the missing FS segment. The sixth band in $Co_{1/3}NbS_2$ develops much stronger dispersion in the direction perpendicular to layers than any other band in $2H$-NbS2 or $Co_{1/3}NbS_2$ that crosses the Fermi level. The corresponding FS segment is shown in the last row of Fig. 10. This pot-shaped segment of the FS features the significant pot-bottom part where the Fermi velocity points along the *c*-axis direction. Figure 10 also provides insight into the relative importance of Co, Nb, and S orbitals in forming states at the FS. The most interesting fact

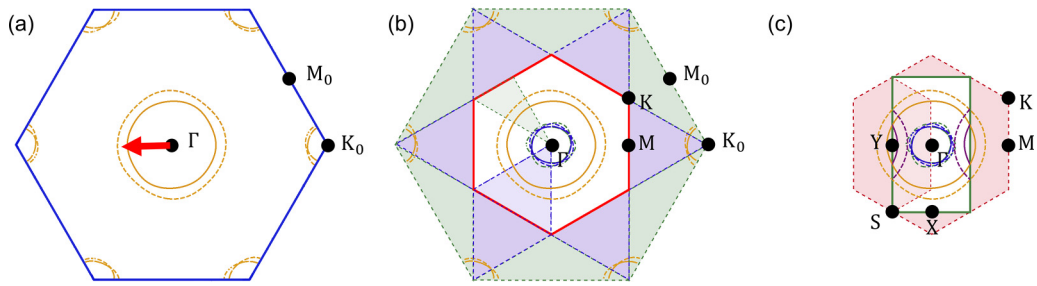

FIG. 12. Schematics of the bands [Fermi surface (FS)] folding form the large hexagonal Brillouin zone (BZ) of $2H$-NbS_2 to the small orthorhombic BZ of $Co_{1/3}NbS_2$ in the $k_z = 0$ cross-section: (a) hexagonal BZ (blue) of $2H$-NbS_2 with the Fermi level that accounts for the charge transfer of 2 electrons/Co from Co to NbS_2 planes. Two branches of FS are visible as full and dotted orange lines. (b) The first hexagonal BZ of $Co_{1/3}NbS_2$ (red hexagon) encompassing six FSs: two orange circles not affected by folding, and four smaller circles, two blue and two green circles, produced folded-in from the second and third BZ, respectively. (c) The first orthorhombic BZ (green rectangle) of antiferromagnetic (AFM)-ordered $Co_{1/3}NbS_2$ with FS branches folded from the crystallographic first BZ (red). Four smaller FS branches are unaffected by the last folding, whereas the large orange branches are partially folded. The Fermi wave number corresponding to the arrow in (a) is characteristic of the almost circular FS of the uniformly doped NbS_2 layer.

to observe in Fig. 10 is that the contribution of Co orbitals to states at the FS, relatively low in general, maximizes in the pot-bottom part of the pot-shaped segment of the FS. That is also the only significant part of the FS with a substantial z-axis component of the Fermi velocity, likely to contribute to the electric conductivity in a direction perpendicular to layers. The high intensity of sulfur contribution in the same region suggests that the Nb-S-Co-S-Nb link provides a relatively important conducting channel for the c-axis electronic transport.

These observations come atop the largest share belonging to Nb2 (niobium atoms positioned right above or below the intercalated Co ions) orbitals. Their share approximately doubles the one belonging to Nb1 (niobium atoms with no Co ions above or below them in the crystal structure) orbitals, a mere consequence of the crystal structure containing twice as many Nb2 atoms than Nb1 atoms. It may also be noted that the total contribution of S orbitals is comparable with that of Nb1. In turn, the shares per atom are comparable for S and Co ions. However, the respective contributions per atom are not comparable, as S atoms are sixfold more abundant in the crystal than Nb1 atoms.

An alternative way to compare the calculated electronic structure in $Co_{1/3}NbS_2$ and $2H$-NbS_2 was recently used in Ref. [12]. Instead of folding the $2H$-NbS_2 spectra into the 1BZ of $Co_{1/3}NbS_2$, the DFT-calculated electronic spectra of magnetically ordered $Co_{1/3}NbS_2$ were unfolded into the six times larger 1BZ of $Co_{1/3}NbS_2$. However, the focus on interest was not the same as here, including the considerations related to electronic transport, which are of important concerns in this paper.

APPENDIX B: ELECTRONIC STRUCTURE IN Co-DEFORMED $2H$-NbS_2 CRYSTAL

To deconstruct the sources of differences in electronic structures of $2H$-NbS_2 and $Co_{1/3}NbS_2$, we have calculated electronic spectra for several auxiliary/artificial crystals. Here, we show the electronic structure for the NbS_2 crystal, conveniently labeled d-NbS_2, where niobium and sulfur atoms are positioned identically as in (DFT relaxed) $Co_{1/3}NbS_2$ crystal. The charge transfer from Co to NbS_2 layers is simulated by including two additional electrons per three NbS_2 formula units into the calculation, whereas the overall charge neutrality is maintained by adding an appropriate homogenous background charge. Regarding the NbS_2 planes, the difference concerning the situation experienced in $Co_{1/3}NbS_2$ is twofold: Co orbitals are not present to hybridize with, and the Coulomb potential of Co^{2+} ions that strongly varies within the unit (super-)cell in $Co_{1/3}NbS_2$ is replaced by the energy offset produced by homogeneously distributed background charge.

The results of the calculation are shown in Fig. 13. The bands that cross the Fermi level along the $\Gamma-X$ line in Fig. 13 can be easily related to those appearing in $Co_{1/3}NbS_2$ and $2H$-NbS_2 (Sec. IV B and Appendix A). The bands that meet the Γ point at 1.1 and 0.1 eV in Fig. 13 correspond to those already present in the same part of the BZ in $2H$-NbS_2 (original-Γ states). Their splitting at the Γ point is substantially bigger than in $2H$-NbS_2 [Fig. 7(a)], indicating a bigger interlayer overlap in d-NbS_2 than in $2H$-NbS2. The change is partly related to the smaller c-axis lattice constant in d-NbS_2. The splitting between bands increases in $Co_{1/3}NbS_2$

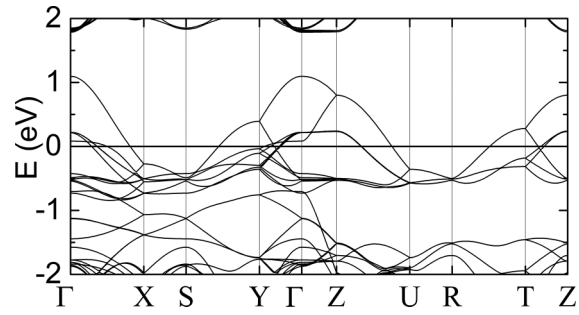

FIG. 13. The calculated electronic band structure for the d-NbS_2 crystal structure, where niobium and sulfur atoms are positioned identically as in $Co_{1/3}NbS_2$.

[see Fig. 7(b)], indicating further interlayer hybridization occurring through Co orbitals. It should be noted that the band structure of d-NbS_2 does not show the potlike 3D FS of $Co_{1/3}NbS_2$ discussed in Appendix A.

The bundle of bands meeting the Γ point around 0.2 eV in Fig. 13 relates to the bundle of bands around the K point in $2H$-NbS_2 [Fig. 7(a)]. In addition to being formally folded to the Γ point in $Co_{1/3}NbS_2$, these states also experience a relative shift in energy relative to the original-Γ states. The shift is accompanied by sizable electron transfer between K and Γ pockets, as first noted in the ARPES experiments in Ref. [106].

In conclusion, examining the d-NbS_2 fictitious crystal helps to identify the sources of changes in the electronic structure $2H$-NbS_2 upon Co intercalation. It also points to the limits of the rigid-band approximation as the most straightforward approach to the electronic structure of $Co_{1/3}NbS_2$.

APPENDIX C: SCHEMATIC C-AXIS TRANSPORT

Here, we provide a detailed explanation of how the arrangement of Co magnetic moments between layers

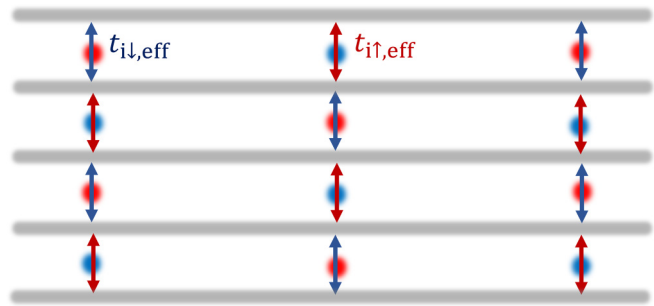

FIG. 14. The schematic representation of dominant interlayer hybridization in the magnetically ordered state. The NbS_2 metallic layers are shown as thick horizontal gray lines with soft edges. The red and soft blue balls represent Co ions in spin-up and spin-down magnetic states. The double arrows in red and blue stand for locally enhanced hybridizations in the spin-up and spin-down channels, respectively. Of course, the two-dimensional (2D) representation, made here for simplicity, cannot faithfully reflect the three-dimensional (3D) atomic structure of $Co_{1/3}NbS_2$, nor its hexagonal order of the first kind (HOFK) magnetic state. The essential features captured by the drawing are the average antiferromagnetic characters of the interlayer and the intralayer orderings.

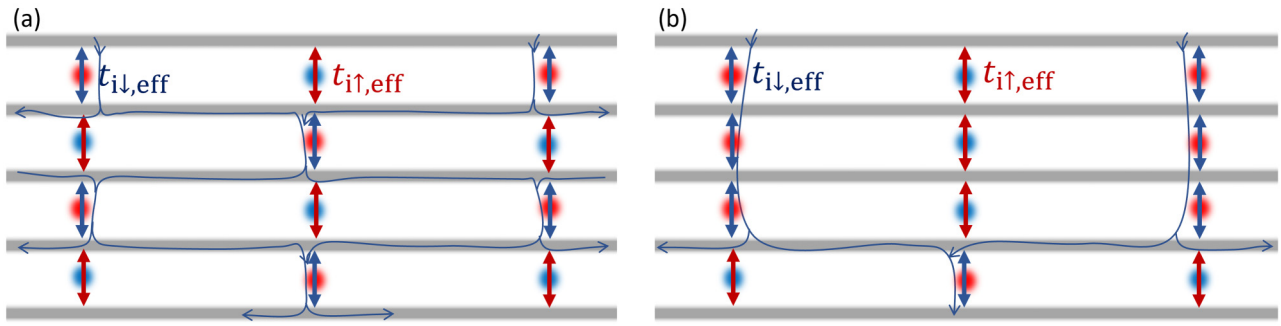

FIG. 15. The conduction paths that (spin-down) electrons take in the electric field perpendicular to layers: (a) in the magnetically ordered state in $Co_{1/3}NbS_2$ and (b) in the state where the magnetic order is locally disrupted. For example, we flip the magnetic moments at three Co ions in the second layer from the top. The meanings of symbols are the same as in Fig. 14. The paths of electrons are shown in curved blue lines. The arrows indicate the direction of electron propagation carrying the current along the *c*-axis direction. In the magnetically ordered state, the electron must travel larger in-plane sections before taking advantage of a suitable interlayer tunneling bridge provided by a Co ion. A local disruption in magnetic order along the *c*-axis direction provides shorter paths with less in-plane scattering.

influences the electronic transport along the *c*-axis direction. To begin, we revisit the magnetic ordering, which has been discussed in Ref. [46] and visualized in Fig. 1(b). In the HOFK state, each Co ion is surrounded by six nearest neighbors within the same layer. Among these neighbors, four have their magnetic moments oriented in the opposite direction to the referent ion, while two have their magnetic moments aligned in the same direction. Additionally, each Co ion has three nearest neighbors in each adjacent layer. Among these neighbors, two have their magnetic moments oriented in the same direction as the referent ion, while one has its magnetic moment oriented in the opposite direction.

If we consider the central Co ion to be in a spin-up state, then according to Fig. 11, only spin-down electrons will benefit from Co-assisted transport. When the spin-down electron arrives in the next layer, to continue along the *c* axis, it needs to find its following spin-up Co ion. However, as mentioned above, it can use only one of the three closest Co ions or make a larger detour in the plane. That suppresses the transport along the *c* axis in the ordered state compared with the disordered state where the probabilities of finding a Co ion in each spin state are equal. The situation is schematically illustrated in Fig. 14.

Figure 15 qualitatively explains why the *c*-axis resistivity in the material increases upon ordering or decreases as the magnetic ordering loses coherence. In essence, for electrons of any spin projection, the AFM-ordering tends to misalign the Co-created tunneling bridges along the *c*-axis direction. In the HOFK magnetically ordered state, the electron of any spin projection is obliged to travel longer sections within planes before taking advantage of Co-created interlayer tunneling bridges [Fig. 15(a)]. The disruptions of the magnetically ordered state bring in the shortcuts along the *c*-axis direction [Fig. 15(b)], leading to shorter effective paths and lower resistivity.

[1] J. A. Wilson, F. J. Di Salvo, and S. Mahajan, Adv. Phys. **24**, 117 (1975).
[2] R. H. Friend, A. R. Beal, and A. D. Yoffe, Philos. Mag. **35**, 1269 (1977).
[3] A. K. Geim and I. V. Grigorieva, Nature (London) **499**, 419 (2013).
[4] Q. H. Wang, K. Kalantar-Zadeh, A. Kis, J. N. Coleman, and M. S. Strano, Nat. Nanotechnol. **7**, 699 (2012).
[5] B. Radisavljevic, A. Radenovic, J. Brivio, V. Giacometti, and A. Kis, Nat. Nanotechnol. **6**, 147 (2011).
[6] E. Morosan, H. W. Zandbergen, B. S. Dennis, J. W. G. Bos, Y. Onose, T. Klimczuk, A. P. Ramirez, N. P. Ong, and R. J. Cava, Nat. Phys. **2**, 544 (2006).
[7] A. F. Kusmartseva, B. Sipos, H. Berger, L. Forró, and E. Tutiš, Phys. Rev. Lett. **103**, 236401 (2009).
[8] B. Sipos, A. F. Kusmartseva, A. Akrap, H. Berger, L. Forró, and E. Tutiš, Nat. Mater. **7**, 960 (2008).
[9] C. Monney, C. Battaglia, H. Cercellier, P. Aebi, and H. Beck, Phys. Rev. Lett. **106**, 106404 (2011).
[10] L. Stojchevska, I. Vaskivskyi, T. Mertelj, P. Kusar, D. Svetin, S. Brazovskii, and D. Mihailovic, Science **344**, 177 (2014).
[11] N. J. Ghimire, A. S. Botana, J. S. Jiang, J. Zhang, Y.-S. Chen, and J. F. Mitchell, Nat. Commun. **9**, 3280 (2018).
[12] P. Popčević, Y. Utsumi, I. Biało, W. Tabis, M. A. Gala, M. Rosmus, J. J. Kolodziej, N. Tomaszewska, M. Garb, H. Berger *et al.*, Phys. Rev. B **105**, 155114 (2022).
[13] M. Naito and S. Tanaka, J. Phys. Soc. Jpn. **51**, 219 (1982).
[14] R. H. Friend and A. D. Yoffe, Adv. Phys. **36**, 1 (1987).
[15] E. A. Marseglia, Int. Rev. Phys. Chem. **3**, 177 (1983).
[16] F. R. de Boer, J. C. P. Klaasse, P. A. Veenhuizen, A. Böhm, C. D. Bredl, U. Gottwick, H. M. Mayer, L. Pawlak, U. Rauchschwalbe, H. Spille *et al.*, J. Magn. Magn. Mater. **63**, 91 (1987).
[17] E. Bauer, E. Gratz, and C. Schmitzer, J. Magn. Magn. Mater. **63**, 37 (1987).
[18] B. Coqblin, M. D. Núñez-Regueiro, A. Theumann, J. R. Iglesias, and S. G. Magalhães, Philos. Mag. **86**, 2567 (2006).

[19] D. Kaczorowski and A. Ślebarski, Phys. Rev. B **81**, 214411 (2010).

[20] M. B. Gamża, R. Gumeniuk, U. Burkhardt, W. Schnelle, H. Rosner, A. Leithe-Jasper, and A. Ślebarski, Phys. Rev. B **95**, 165142 (2017).

[21] R. Peters and N. Kawakami, Phys. Rev. B **96**, 115158 (2017).

[22] M. Shahzad and P. Sengupta, Phys. Rev. B **96**, 224402 (2017).

[23] H. Gretarsson, A. Lupascu, J. Kim, D. Casa, T. Gog, W. Wu, S. R. Julian, Z. J. Xu, J. S. Wen, G. D. Gu *et al.*, Phys. Rev. B **84**, 100509(R) (2011).

[24] B. Fauqué, Y. Sidis, V. Hinkov, S. Pailhès, C. T. Lin, X. Chaud, and P. Bourges, Phys. Rev. Lett. **96**, 197001 (2006).

[25] Y. Li, V. Balédent, N. Barišić, Y. Cho, B. Fauqué, Y. Sidis, G. Yu, X. Zhao, P. Bourges, and M. Greven, Nature (London) **455**, 372 (2008).

[26] S. De Almeida-Didry, Y. Sidis, V. Balédent, F. Giovannelli, I. Monot-Laffez, and P. Bourges, Phys. Rev. B **86**, 020504(R) (2012).

[27] N. Barišić, S. Badoux, M. K. Chan, C. Dorow, W. Tabis, B. Vignolle, G. Yu, J. Béard, X. Zhao, C. Proust *et al.*, Nat. Phys. **9**, 761 (2013).

[28] N. Barišić, M. K. Chan, Y. Li, G. Yu, X. Zhao, M. Dressel, A. Smontara, and M. Greven, Proc. Natl. Acad. Sci. USA **110**, 12235 (2013).

[29] M. K. Chan, M. J. Veit, C. J. Dorow, Y. Ge, Y. Li, W. Tabis, Y. Tang, X. Zhao, N. Barišić, and M. Greven, Phys. Rev. Lett. **113**, 177005 (2014).

[30] A. J. Drew, C. Niedermayer, P. J. Baker, F. L. Pratt, S. J. Blundell, T. Lancaster, R. H. Liu, G. Wu, X. H. Chen, I. Watanabe *et al.*, Nat. Mater. **8**, 310 (2009).

[31] Z. P. Yin, K. Haule, and G. Kotliar, Nat. Phys. **7**, 294 (2011).

[32] R. Moessner and A. P. Ramirez, Phys. Today **59**, 24 (2006).

[33] N. Barišić, D. Wu, M. Dressel, L. J. Li, G. H. Cao, and Z. A. Xu, Phys. Rev. B **82**, 054518 (2010).

[34] K. Motizuki, H. Ido, T. Itoh, and M. Morifuji, *Electronic Structure and Magnetism of 3d-Transition Metal Pnictides* (Springer, Berlin, 2010).

[35] T. Park, F. Ronning, H. Q. Yuan, M. B. Salamon, R. Movshovich, J. L. Sarrao, and J. D. Thompson, Nature **440**, 65 (2006).

[36] S. Wirth and F. Steglich, Nat. Rev. Mater. **1**, 16051 (2016).

[37] T. Takeuchi, S. Hashimoto, T. Yasuda, H. Shishido, T. Ueda, M. Yamada, Y. Obiraki, M. Shiimoto, H. Kohara, T. Yamamoto *et al.*, J. Phys.: Condens. Matter **16**, L333 (2004).

[38] S. Nair, O. Stockert, U. Witte, M. Nicklas, R. Schedler, K. Kiefer, J. D. Thompson, A. D. Bianchi, Z. Fisk, S. Wirth *et al.*, Proc. Natl. Acad. Sci. USA **107**, 9537 (2010).

[39] P. Gegenwart, Q. Si, and F. Steglich, Nat. Phys. **4**, 186 (2008).

[40] K. Anzenhofer, J. M. Van Den Berg, P. Cossee, and J. N. Helle, J. Phys. Chem. Solids **31**, 1057 (1970).

[41] S. S. P. Parkin and R. H. Friend, Philos. Mag. B **41**, 65 (1980).

[42] A. A. Aczel, L. M. DeBeer-Schmitt, T. J. Williams, M. A. McGuire, N. J. Ghimire, L. Li, and D. Mandrus, Appl. Phys. Lett. **113**, 032404 (2018).

[43] N. Suzuki, Y. Yamazaki, T. Teshima, and K. Motizuki, Phys. B Phys. **156**, 286 (1989).

[44] Y. Kousaka, Y. Nakao, J. Kishine, M. Akita, K. Inoue, and J. Akimitsu, Nucl. Instrum. Methods Phys. Res. A **600**, 250 (2009).

[45] T. Moriya and T. Miyadai, Solid State Commun. **42**, 209 (1982).

[46] S. S. P. Parkin, E. A. Marseglia, and P. J. Brown, J. Phys. C: Solid State Phys. **16**, 2765 (1983).

[47] M. Nakayama, K. Miwa, H. Ikuta, H. Hinode, and M. Wakihara, Chem. Mater. **18**, 4996 (2006).

[48] G. Tenasini, E. Martino, N. Ubrig, N. J. Ghimire, H. Berger, O. Zaharko, F. Wu, J. F. Mitchell, I. Martin, L. Forró *et al.*, Phys. Rev. Res. **2**, 023051 (2020).

[49] N. Barišić, I. Smiljanić, P. Popčević, A. Bilušić, E. Tutiš, A. Smontara, H. Berger, J. Jaćimović, O. Yuli, and L. Forró, Phys. Rev. B **84**, 075157 (2011).

[50] X. P. Yang, H. LaBollita, Z.-J. Cheng, H. Bhandari, T. A. Cochran, J.-X. Yin, M. S. Hossain, I. Belopolski, Q. Zhang, Y. Jiang *et al.*, Phys. Rev. B **105**, L121107 (2022).

[51] H. Tanaka, S. Okazaki, K. Kuroda, R. Noguchi, Y. Arai, S. Minami, S. Ideta, K. Tanaka, D. Lu, M. Hashimoto *et al.*, Phys. Rev. B **105**, L121102 (2022).

[52] F. Jellinek, G. Brauer, and H. Müller, Nature **185**, 376 (1960).

[53] CrysAlisPro, Rigaku Oxford Diffraction (2017), version: 1.171.39.13a, Rigaku Corporation, Oxford, UK.

[54] Although the literature concerning lattice constants of $Co_{1/3}NbS_2$ and $2H$-NbS_2 is not entirely consistent, the compound intercalated with 33% of Co shows statistically the same lattice constants as the parent compound [47,52,107–111]. Several studies show that the c-axis lattice constant increases with increasing the concentration of Co, Mn, and Li intercalants. The extrapolation to low concentration of intercalated ions indicates the initial shrinking of the c-axis lattice constant upon intercalation, followed by a monotonic increase at higher levels of intercalation [47,109,112]. For reference, the reported c-axis lattice constant of the parent compound ranges from 1.188 to 1.196 nm [52,110–112].

[55] P. J. W. Moll, The role of anisotropy in iron-pnictides addressed by focused ion beam sample fabrication, Ph.D. Thesis, ETH Zurich (2012).

[56] S. Arsenijević, C. Petrovic, L. Forró, and A. Akrap, Europhys. Lett. **103**, 57015 (2013).

[57] S. Klotz, G. Hamel, and J. Frelat, High Press. Res. **24**, 219 (2004).

[58] Đ. Drobac and Ž. Marohnić, Fiz. A **8**, 165 (1999).

[59] P. Giannozzi, O. Andreussi, T. Brumme, O. Bunau, M. Buongiorno Nardelli, M. Calandra, R. Car, C. Cavazzoni, D. Ceresoli, M. Cococcioni *et al.*, J. Phys.: Condens. Matter **29**, 465901 (2017).

[60] A. Dal Corso, Comput. Mater. Sci. **95**, 337 (2014).

[61] J. P. Perdew, K. Burke, and M. Ernzerhof, Phys. Rev. Lett. **77**, 3865 (1996).

[62] N. Marzari, D. Vanderbilt, A. De Vita, and M. C. Payne, Phys. Rev. Lett. **82**, 3296 (1999).

[63] M. Cococcioni and S. de Gironcoli, Phys. Rev. B **71**, 035105 (2005).

[64] I. Timrov, N. Marzari, and M. Cococcioni, Phys. Rev. B **98**, 085127 (2018).

[65] Y. Horibe, J. Yang, Y.-H. Cho, X. Luo, S. B. Kim, Y. S. Oh, F.-T. Huang, T. Asada, M. Tanimura, D. Jeong *et al.*, J. Am. Chem. Soc. **136**, 8368 (2014).

[66] E. Martino, C. Putzke, M. König, P. J. W. Moll, H. Berger, D. LeBoeuf, M. Leroux, C. Proust, A. Akrap, H. Kirmse *et al.*, npj 2D Mater. Appl. **5**, 86 (2021).

[67] G. Knebel, D. Aoki, and J. Flouquet, Comptes Rendus Phys. **12**, 542 (2011).

[68] N. W. Ashcroft and N. D. Mermin, *Solid State Physics* (Saunders College Publishers, New York, 1976), Chap. 31, p. 656.

[69] A. P. Ramirez, Annu. Rev. Mater. Sci. **24**, 453 (1994).

[70] The slight discrepancy in the *c*-axis FC magnetic susceptibility between data presented here and those published in Refs. [2,11] is possibly related to the variation in sample quality.

[71] S. Mangelsen, P. Zimmer, C. Näther, S. Mankovsky, S. Polesya, H. Ebert, and W. Bensch, Phys. Rev. B **103**, 184408 (2021).

[72] P. Park, Y.-G. Kang, J. Kim, K. H. Lee, H.-J. Noh, M. J. Han, and J.-G. Park, npj Quantum Mater. **7**, 42 (2022).

[73] I. Dzyaloshinsky, J. Phys. Chem. Solids **4**, 241 (1958).

[74] The Co ions are too far apart for direct exchange interaction to occur [41].

[75] Y. Togawa, J. Kishine, P. A. Nosov, T. Koyama, G. W. Paterson, S. McVitie, Y. Kousaka, J. Akimitsu, M. Ogata, and A. S. Ovchinnikov, Phys. Rev. Lett. **122**, 017204 (2019).

[76] D. W. Woodard and G. D. Cody, Phys. Rev. **136**, A166 (1964).

[77] P. B. Allen, W. E. Pickett, K. M. Ho, and M. L. Cohen, Phys. Rev. Lett. **40**, 1532 (1978).

[78] T. Hagino, Y. Seki, N. Wada, S. Tsuji, T. Shirane, K. I. Kumagai, and S. Nagata, Phys. Rev. B **51**, 12673 (1995).

[79] A. T. Burkov, T. Nakama, M. Hedo, K. Shintani, K. Yagasaki, N. Matsumoto, and S. Nagata, Phys. Rev. B **61**, 10049 (2000).

[80] E. Bauer, X.-Q. Chen, P. Rogl, G. Hilscher, H. Michor, E. Royanian, R. Podloucky, G. Giester, O. Sologub, and A. P. Gonçalves, Phys. Rev. B **78**, 064516 (2008).

[81] A. Akrap, E. Tutiš, S. M. Kazakov, N. D. Zhigadlo, J. Karpinski, and L. Forró, Phys. Rev. B **75**, 172501 (2007).

[82] L. Rebelsky, K. Reilly, S. Horn, H. Borges, J. D. Thompson, and R. Caspary, J. Appl. Phys. **67**, 5206 (1990).

[83] M. Inoue, Y. Muneta, H. Negishi, and M. Sasaki, J. Low Temp. Phys. **63**, 235 (1986).

[84] Other parameters are $\rho_0 = (150.0 \pm 1)$ μΩ cm, $\rho_1 = (45 \pm 3)$ μΩ cm, and $\rho_2 = (105 \pm 3)$ μΩ cm.

[85] The behavior observed in $\rho_{ab}(T)$ at a pressure around 1 GPa superficially resembles the behavior observed in the Kondo lattice systems [113,114].

[86] J. J. Barry and H. P. Hughes, J. Phys. C: Solid State Phys. **16**, 5393 (1983).

[87] A. Juhin, F. de Groot, G. Vankó, M. Calandra, and C. Brouder, Phys. Rev. B **81**, 115115 (2010).

[88] J. Chen, X. Wu, and A. Selloni, Phys. Rev. B **83**, 245204 (2011).

[89] G. W. Mann, K. Lee, M. Cococcioni, B. Smit, and J. B. Neaton, J. Chem. Phys. **144**, 174104 (2016).

[90] N. Sirica, S.-K. Mo, F. Bondino, I. Pis, S. Nappini, P. Vilmercati, J. Yi, Z. Gai, P. C. Snijders, P. K. Das *et al.*, Phys. Rev. B **94**, 075141 (2016).

[91] N. Sirica, P. Vilmercati, F. Bondino, I. Pis, S. Nappini, S.-K. Mo, A. V. Fedorov, P. K. Das, I. Vobornik, J. Fujii *et al.*, Commun. Phys. **3**, 65 (2020).

[92] Z. El Youbi, S. W. Jung, C. Richter, K. Hricovini, C. Cacho, and M. D. Watson, Phys. Rev. B **103**, 155105 (2021).

[93] M. Kawamura, Comput. Phys. Commun. **239**, 197 (2019).

[94] Alternatively, one may consider the DFT-calculated effective spin value of 1.18 to be a mixture of spin $S = \frac{3}{2}$ and 1 states, in relative proportions of 36.3 and 63.7%. This type of averaging produces a similar value for the effective magnetic moment, $2\mu_B \sqrt{\langle S(S+1)\rangle} = 3.25\mu_B$, this time ∼3% bigger than the measured value of $(\sqrt{\langle \vec{\mu}^2 \rangle})_{\text{exp}} = 3.17\mu_B$. Both comparisons lead to numerically similar results, with no reasons to prefer one.

[95] M. Mito, T. Tajiri, K. Tsuruta, H. Deguchi, J. Kishine, K. Inoue, Y. Kousaka, Y. Nakao, and J. Akimitsu, J. Appl. Phys. **117**, 183904 (2015).

[96] L. Ehm, K. Knorr, L. Peters, S. Rath, and W. Depmeier, J. Alloys Compd. **429**, 82 (2007).

[97] R. E. Jones, H. R. Shanks, D. K. Finnemore, and B. Morosin, Phys. Rev. B **6**, 835 (1972).

[98] S. Doniach, Physica B+C **91**, 231 (1977).

[99] See Supplemental Material at http://link.aps.org/supplemental/10.1103/PhysRevB.107.235149 for detailed discussion and calculation of the RKKY interaction in $Co_{1/3}NbS_2$.

[100] D. M. Cragg and P. Lloyd, J. Phys. C: Solid State Phys. **12**, L215 (1979).

[101] P. Nozières and A. Blandin, J. Phys. **41**, 193 (1980).

[102] N. Andrei and C. Destri, Phys. Rev. Lett. **52**, 364 (1984).

[103] J. Gan, P. Coleman, and N. Andrei, Phys. Rev. Lett. **68**, 3476 (1992).

[104] Y. Motome, K. Nakamikawa, Y. Yamaji, and M. Udagawa, Phys. Rev. Lett. **105**, 036403 (2010).

[105] S. Polesya, S. Mankovsky, and H. Ebert, Z. Naturforsch. B **74**, 91 (2019).

[106] C. Battaglia, H. Cercellier, L. Despont, C. Monney, M. Prester, H. Berger, L. Forró, M. G. Garnier, and P. Aebi, Eur. Phys. J. B **57**, 385 (2007).

[107] J. M. van den Berg and P. Cossee, Inorg. Chim. Acta **2**, 143 (1968).

[108] W. B. Clark, J. Phys. C: Solid State Phys. **9**, L693 (1976).

[109] A. Le Blanc-Soreau, J. Rouxel, M.-F. Gardette, and O. Gorochov, Mater. Res. Bull. **11**, 1061 (1976).

[110] L. Schmidt, Phys. Lett. A **31**, 551 (1970).

[111] G. A. Wiegers, R. J. Haange, and F. van Bolhuis, Phys. Status Solidi **107**, 817 (1988).

[112] D. C. Dahn, J. F. Carolan, and R. R. Haering, Phys. Rev. B **33**, 5214 (1986).

[113] Y. Ōnuki and T. Komatsubara, J. Magn. Magn. Mater. **63**, 281 (1987).

[114] S. Nakatsuji, S. Yeo, L. Balicas, Z. Fisk, P. Schlottmann, P. G. Pagliuso, N. O. Moreno, J. L. Sarrao, and J. D. Thompson, Phys. Rev. Lett. **89**, 106402 (2002).